BILINGUAL
PUBLISHING CO.
Pioneer of Global Academics Since 1984

Journal of Metallic Material Research

Volume 5 · Issue 1 · April 2022 | ISSN 2630-5135 (Online)

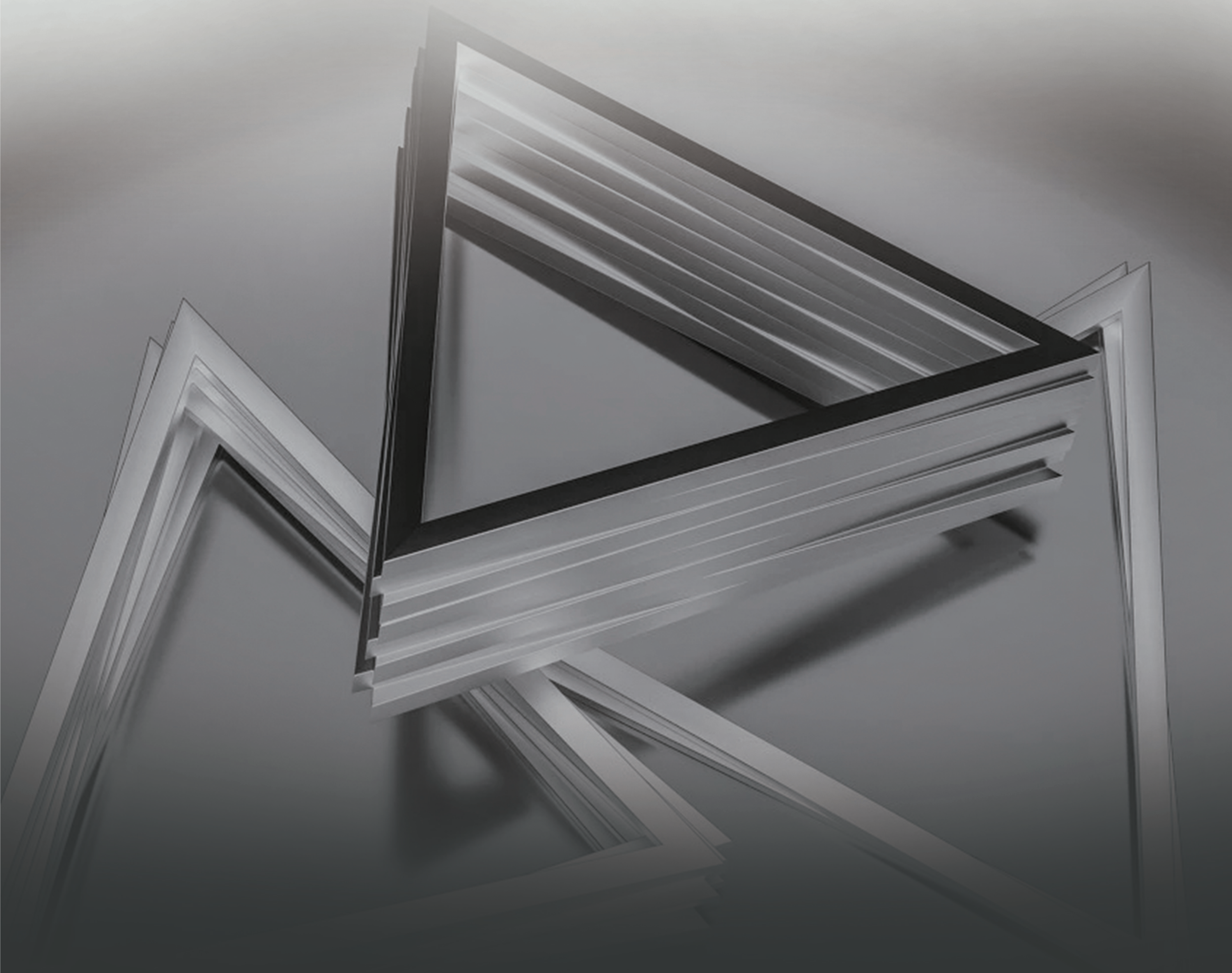

BPC
BILINGUAL
PUBLISHING CO.
Pioneer of Global Academics Since 1984

Editor-in-Chief

Dr.OlegValentinovich
Sobol,Ukraine

Editorial Board Members

Shuo Chen, United States
Changrui Wang, China
Madhukar Eknath Navgire, India
Unal Camdali, Turkey
Jitendra Kumar Singh, Korea
Abhay Nanda Srivastva, India
Vivek Patel, India
Bandar Abdulaziz AlMangour, Saudi Arabia
Soumen Maiti, India
Jonathan David Parker, Canada
Samson jerold samuel Chelladurai, India
Akash Deep Sharma, India
Dan Dobrotă, Romania
Asit Kumar Gain, Australia
Dragica Milan Minic, Serbia
Chandan Pandey, India
Mahnaz Mahdavi Shahri, Iran
Deniz Uçar, Turkey
Weidong Song, China
Attoui Aissa, Algeria
Qiaoli Lin, China
Subravel Visvalingam, India
Asaminew Abiyu Cherinet, Ethiopia
Arif Gök, Turkey
Ning Li, China
Fufa Wu, China
Wenchun Jiang, China
Saeed Zeinali Heris, Iran
Vladimir Victorovich Lukov, Russian Federation
Abhishek Ghosh, India
KangHua Chen, China
Pradeep L Menezes, United States
Naushad Ahmad, India
S Selvam, India
Guocheng Zhu, China
Mohamed Kamal ElFawkhry, India
Mohammad Hassan Shirani Bidabadi, China Mohd
Vladimir Mikhailov Yegorovich, Russian Federation
Robin Gupta, India
Sergey Vasilevich Byvaltsev, Russian Federation
Nitin Saini, India
Ramesh Balakrishnan, India
Alexander Evgenievich Barmin, Ukraine
Khitam Abdulhussein Saeed, Malaysia
Paparao Mondi, India
Zbigniew Ranachowski, Poland
Sami ullah Rather, Saudi Arabia
Shengqiang Ma, China
Md Saiful Islam, Bangladesh
Ajay Kumar Choubey, India
Saeed Kakaei, Iran
Hojat Jafari, Iran
Yuhan Liang, United States
Ahmed Wagih, Egypt
Rong Liu, Canada
Francesco Caridi, Italy
Konstanti Viktorovich Ivanov, Russian Federation
Dipak Kumar, India
Americo Scotti, Brazil
Mohsen Vafaeifard, Malaysia
Hülya - Demirören, Turkey
Tahir Mohiuddin Bhat, India
Hamit Özkan Gülsoy, Turkey
Sandhya Dwevedi, India
Sergey Nikolaevich Lezhnev, Kazakhstan
Faysal Fayez Eliyan, Canada
Shouxun Ji, United Kingdom
Patrice Berthod, France
Moslem Mansour Lakouraj, Iran
Akhyar - Akhyar, Indonesia
Chih-Chun Hsieh, Taiwan
Lutfiddin Omanivich Olimov, Uzbekistan
Mahmoud Ebrahimi, Iran
Murat Sarıkaya, Turkey
Yaofeng Chang, United States
Mehmet Kaya, Turkey
Meilinda Nurbanasari, Indonesia
Rizk Mostafa Shalaby, Egypt
Anatolii Michailovich Lepikhin, Russian Federation

Volume 5 Issue 1 • April 2022 • ISSN 2630-5135 (Online)

Journal of Metallic Material Research

Editor-in-Chief

Dr. Oleg Valentinovich

BILINGUAL
PUBLISHING CO.
Pioneer of Global Academics Since 1984

BILINGUAL PUBLISHING CO.
Pioneer of Global Academics Since 1984

Volume 5 | Issue 1 | April 2022 | Page1-37
Journal of Metallic Material Research

Contents

Articles

Journal of Metallic Material Research
https://ojs.bilpublishing.com/index.php/jmmr

ARTICLE

The Influence of Friction Time on the Joint Interface and Mechanical Properties in Dissimilar Friction Welds

Venkata Charan Kantumuchu[1] **Muralimohan Cheepu**[2*]

1. Electrex Inc. Hutchinson, Kansas, United States
2. Super-TIG Welding Co., Limited, Busan, 46722, Republic of Korea

ARTICLE INFO

Article history
Received: 13 December 2021
Accepted: 7 February 2022
Published Online: 11 February 2022

Keywords:
Friction welding
Microstructure
Dissimilar materials
Stainless steel
Mechanical properties

ABSTRACT

The welding of dissimilar materials is one of the challenging issues in the fabrication industry to obtain required quality welds using fusion welding methods. However, some processes recently improved interface bonding with low joint strength. Unfortunately, the major intermetallic compounds could not alleviate from the joint interface. Alternatively, solid-state welding methods revealed fewer intermetallics at the joint interface for dissimilar material welds. Among them, friction welding was chosen to join incompatible materials with the necessary properties successfully. Friction time is a critical parameter for obtaining strong welds through friction welding, apart from friction pressure, forging pressure, forging time, and rotational speed. Variability of friction time can change the strength of friction by changing mechanical properties such as tensile strength. This change of tensile strength is typically influenced by the intermixing region, dependent on friction time. In this experiment, carbon steel and stainless steel have been friction welded to test the impact of friction time on the joint interface where the substrate's faying surface meets. This interface consists of the intermixing region of the two materials on which the friction welding is performed. The results showed an interesting variation in tensile strength, with varying friction time. The width of the intermixing zone increased gradually with friction time until and decreased with the further increasing. The strength of the welds obtained was the highest of 730 MPa at a friction time of 4 s and fell as friction time's increased value after 4 s.

1. Introduction

Though heat generated during the relative movement of two parts is considered undesirable because of the wear it could cause, it is sometimes used for other applications such as friction welding. Friction welding is a popular welding method for dissimilar metals because of several advantages the welding method offers. Friction welding

---

*Corresponding Author:
Muralimohan Cheepu,
Super-TIG Welding Co., Limited, Busan, 46722, Republic of Korea;
Email: muralicheepu@gmail.com

DOI: https://doi.org/10.30564/jmmr.v5i1.4209

is one of the solid-state welding processes like diffusion bonding, friction stir welding, etc. Solid-state welding processes are quite different from the fusion welding methods to produce the joints with quality. The quality of the joints is likely to depend on the heat input or the temperature of the welds. The joint temperature of the friction welding method is much lower than the other welding processes [1-4]. Therefore, the quality of the welds is uttermost for any kind of materials to be joined. The joining of a similar combination of materials revealed successful metallurgical bonding without defects. Similarly, dissimilar combinations materials were obtained with excellent joint properties [5-8]. Due to the increase in demand for joining dissimilar material combinations in applications such as cryogenic fluids, power generation industries, and reactor cooling systems, solid-state welding is most suitable in the current scenario [9-14]. Friction welding happens due to the heat produced by friction during the movement of two parts. Friction welding (FW) is a class of solid-state welding process that generates heat through mechanical friction between a moving workpiece and a stationary component, with the addition of a lateral force called upset to plastically displace and fuse the materials [15-18]. Because of the nature of the process of welding, the strength of friction welding could vary on different factors. Some of the factors that need to be optimized for efficient frictional welding are friction pressure, friction time, rotational speed, forging pressure, forging time, and burn-off length [19-22].

In addition, some of the studies were identified the relation between metallurgical properties and the mechanical properties of the similar and dissimilar combination of friction welds [23]. It is important to note that the interface of the two joining materials, which is referred to as the intermixing region has an impact on the mechanical properties of the weld. The bonding line and intermixing zones play an important role in the mechanical properties of the joints [24]. Moreover, the welding parameters influence the formation of the weld interface with the necessary strength to attain excellent mechanical properties [25]. Some of the studies reported that the axial shortening of the materials at the interface is affected by the welding conditions [26]. Based on the axial shortening, the joint interface is varied with the presence of intermixing zone. In this experiment, we aim to find how the intermixing region is affected by the various factors involved in friction welding, and specifically, we consider the effect of friction time and how the tensile strength of this weld joint is affected by changing the friction time. It was also reported by some studies on the impact of friction time on the properties of friction welded YSZ-alumina composite and 6061 aluminum alloy, they found that the experimental results showed that the friction time has a significant effect on the joint structure and mechanical properties [27]. In particular, the effect of burn-off length reported being changed the intermixing zone along with axial shortening. A large number of axial shortening joints were revealed with the hardened intermixing zone over the less axial shortening joints [28]. There are some incompatible dissimilar combinations that are unable to join them using fusion welding methods. Unfortunately, the same combination of materials was also not successful to obtain strong joint strength using friction welding [29]. However, the incompatible materials were joined using interlayer techniques inserting them in between the two substrates. For example, the joining of titanium to stainless steel was resulted in brittle joint failure due to the formation of brittle intermetallic layers. Therefore, Ni, V, Ta, Al, and Cu interlayers were used to avoid direct contact between the two materials [30]. Whatever, the joint method either with interlayers or without interlayers, the effect of friction time remains valid to obtain the excellent joint interface to control the joint strength.

Similarly, the studies on the friction welding of AISI 304 and the effect of friction time on microstructure, microhardness, and tension-compression properties were found that with increasing friction time, a hard zone was found at the interface of the welded joint because of extended high plastic deformation zone [31]. Also, in an experiment conducted by Hakan Ates and Nihat Kaya on the effect of friction time on microstructure and mechanical properties of friction welded AISI 304 stainless steel to AISI 1060 steel, the experiment revealed that the tensile strength of friction-welded joints was not affected by friction time. The tensile strength of obtained weld joints can exceed AISI 304SS strength by 30% [32]. Moreover, in an experiment conducted by Ozdemir et al., on the effect of rotational speed on the interface properties of friction-welded AISI 304L to 4340 steel, it was found that the thickness of full plastic deformed zone (FPDZ) formed at the interface was reduced as a result of more mas discarded from the welding interface with the increase of rotational speed [33].

The aim of this study is to investigate the influence of friction time on the dissimilar materials of stainless steel to carbon steel friction weld's tensile strength. The correlation between metallurgical and mechanical properties was also determined and analyzed with the friction time to obtain the required joint strength.

2. Experimental Procedure

In this study, austenitic stainless steel and carbon steel materials with the dimensions of 14 mm in diameter and 120 mm in length rods were used. The faying surfaces of the substrates were machined and cleaned before performing the welds. The weld surfaces were polished to get the required surface roughness, which has a more significant effect on the enhancement of joint strength. A continuous drive friction welding machine with a capacity of 200 kN of ETA make was used to make the friction welds. The process parameters have a more significant effect in the friction welding process to obtain the sound welds between dissimilar materials. The process parameters such as friction time, friction pressure, upset force, upset time, and rotational speed have a direct relation to the formation of joint and on its strength. To achieve the higher tensile strength of the welds, a new set of welding parameters were intended after the several experimental trails of the welds with varying the friction time from 1 s to 6 s, and other parameters were kept as constant with a friction pressure of 110 MPa, upset pressure of 240 MPa, upset time of 5 s and the rotational speed of 1500 rpm. Friction welded joints were cut into cross sections for metallographic sample preparations. To evaluate the mechanical properties of the joints, tensile and fatigue test samples were prepared as per the ASTM E8 standard. The tensile tests were performed on the universal testing machine of the TFUC-400 model. The joint interface microstructural observations were characterized by an optical microscope, scanning electron microscope (SEM). To reveal the microstructural features of the welds, polished surfaces were etched with 2% nital solution on the carbon steel side and an aqua-regia solution on the stainless steel side was used.

3. Results and Discussion

Dissimilar materials of austenitic stainless steel to carbon steel have joined using friction welding by varying friction time. Friction time is a significant parameter for generating the required heat to weld the materials. The selected materials in this study are almost hard and need to produce sufficient heat at the interface to obtain the necessary joint properties. It has been identified from the experimental results that friction time is a dominant parameter compared to others for this combination of materials. The impact of friction time on the weld interface and weld flash are also determined. Figure 1 illustrates the macrostructure of the friction welded joint with an interface and weld flash. The weld flash on the carbon steel side is higher than the stainless steel. It is due to that the yield strength of the carbon steel is much lower than the stainless steel that too at high temperature, it is much lower than the room temperature. Therefore, the deformed weld flash on carbon steel is more extensive than stainless steel. In addition, the weld interface is slightly irregular on the carbon steel side with deformed notches. The detailed observations of the weld interface have been examined in microstructures. Figure 2 indicated the formation of intermixing zone in with the carbon steel bands at different friction times. The dark-colored islands in the stainless steel matrix belong to the carbon steel, which is mixed during welding. The width of the intermixing zone was occupied with the more prominent bands of carbon steel. It is owing to the interchanging of softened metal at the interface during friction time with the rubbing action of faying surfaces. Figure 2b confirms that the weld interface is strongly bonded metallurgically without defects. It is worth mentioning the effect of friction time on the weld interface. In Figure 2, it is clearly indicated that the increase of intermixing zone as increasing friction time. In general, the weld interface examines to conform to the interface bonding and other defects caused by insufficient heat and pressure. The quantitative analysis of the intermixing zone between carbon steel and stainless steel has been determined according to the friction time depicted in Figure 3. It revealed that the remarkable trend between friction time and intermixing zone with the polynomial fitted curve R^2 is 0.99. The width of the intermixed zone increases with the increasing friction time. The effect of friction time until 4 s is not dominant to produce a broad intermixing region.

In contrast, the intermixing zone increased drastically with increasing friction time by more than 4 s. In addition, the weld interface becomes asymmetrical if the friction time raises further to 7 s. Therefore, the maximum friction time of 6 s was used for the selected dissimilar combination of materials. Intermixing zone consisting of hard and soft layers which belong to stainless steel and carbon steel, respectively. During friction welding, due to the action of angular velocity, the softened material from the carbon steel tries to go away from the center to the periphery of the joint. At this instance, some of the material remains in the central region and is mixed with the opposite matrix. Therefore, the intermixing region is directly related to the friction time up to some level and it also depends on the certain combination of materials.

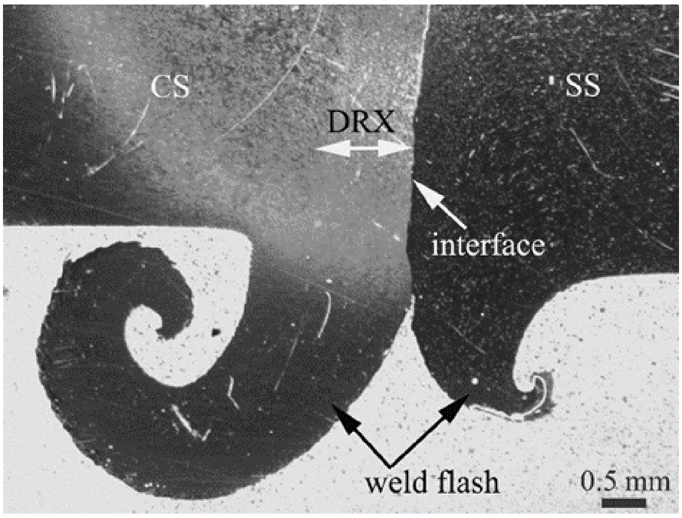

Figure 1. Macrostructure of the dissimilar friction welds with different amounts of weld flash.

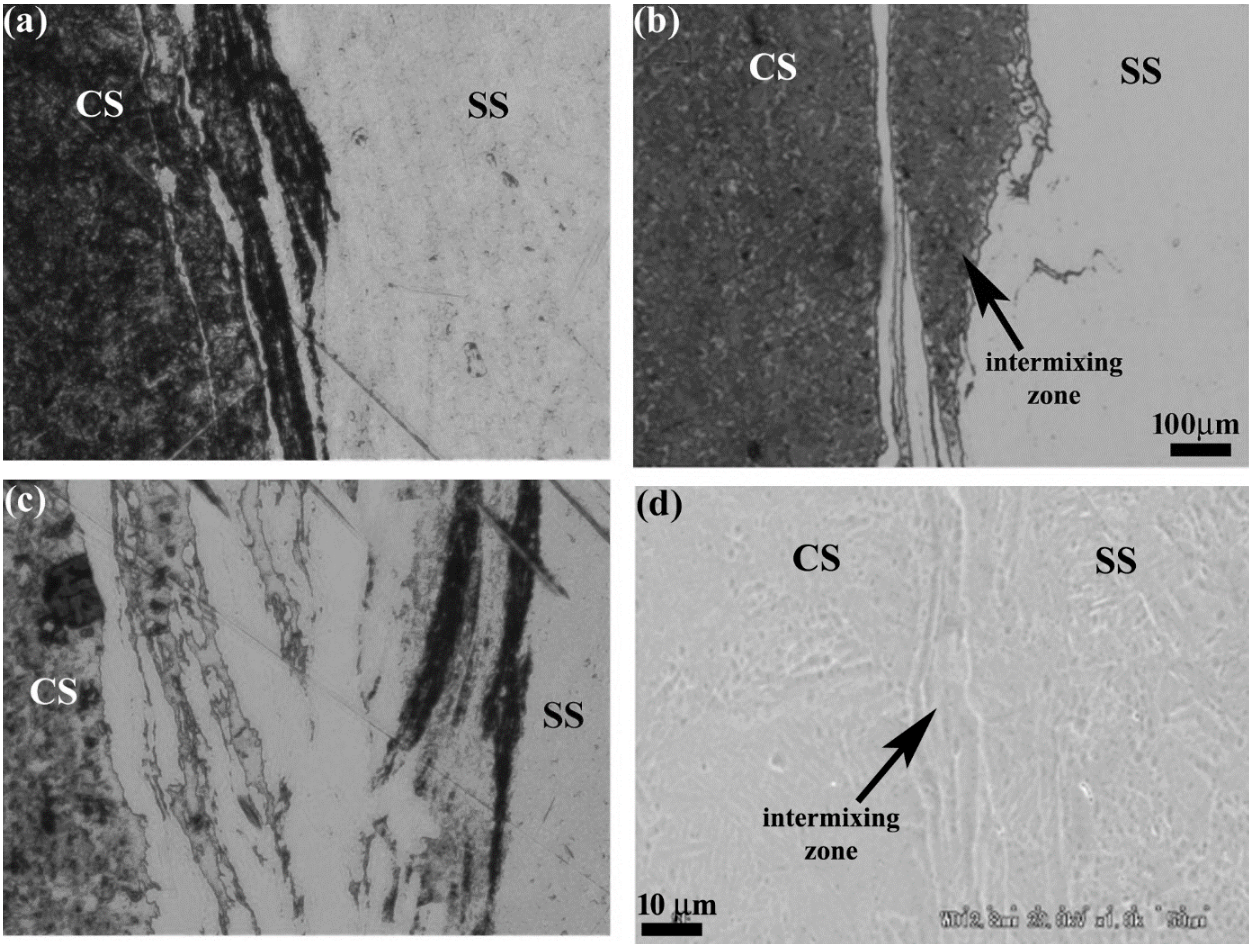

Figure 2. Microstructures show the weld interface with intermixing zone at friction time of (a) 1 s, (b) 3 s (c) 6 s, and (d) enlarged view of (b).

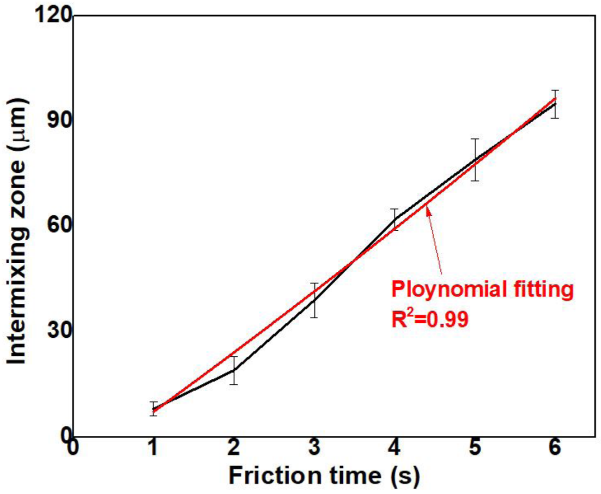

Figure 3. The relation between friction time and intermixing zone with the polynomial fitting curve.

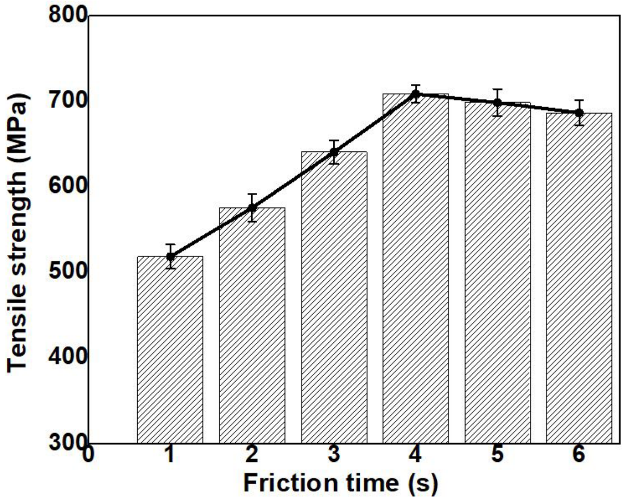

Figure 4. The effect of friction time on the tensile strength of the dissimilar friction welds

It is essential to analyze the intermixing zone and its characteristics with the mechanical properties of the welds. As mentioned earlier, the microhardness tests confirmed that the hard and soft later in the intermixing regions. But the mechanical properties dramatically depend on the width of intermixing zone. Figure 4 represents the joint tensile strength according to the friction time. The strength of the welds increases gradually with the increase of friction time until 4 s, while the strength of the welds decreases with the further increase of friction time. In the correlation study between the intermixing zone and the tensile strength concerning friction time, the maximum tensile strength was obtained at a width of the intermixing zone is about 65 μm. Figure 5 illustrates the fracture morphology of the tensile fractured surfaces with the ductile mode of fracture. The fracture surfaces confirmed that the welds were free from the cracks.

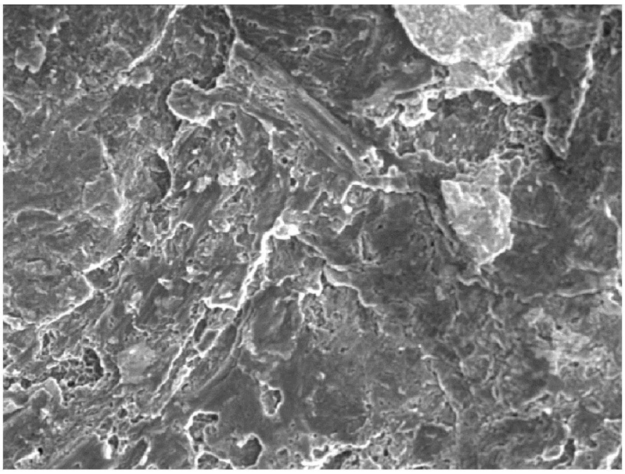

Figure 5. SEM analysis of the tensile fracture surface with ductile mode of failure.

4. Conclusions

The dissimilar materials of stainless steel to carbon steel have been friction welded to study the effect of friction time on the tensile strength of the welds. Based on the presented results, the following conclusions are drawn:

- The range of friction time from 1 s to 6 s was determined as suitable for the friction welding of carbon steel to stainless steel welds.
- The width of the intermixing zone increased gradually with friction time along with the axial shortening.
- The strength of the welds obtained was the highest of 730 MPa at a friction time of 4 s. The further increase of friction time after 4 s resulted in decreasing in joint strength.
- As a result of friction time the maximum tensile strength was obtained at a width of the intermixing zone is about 65 μm.
- The softened carbon steel materials diffused toward the stainless steel within the intermixed zone during the friction stage.

References

[1] Shanjeevi, C., Arputhabalan, J.J., Dutta, R., 2017. Investigation on the Effect of Friction Welding Parameters on Impact Strength in Dissimilar Joints. IOP Conference Series: Materials Science and Engineering. 197(1), 012069.

[2] Cheepu, M., Susila, P., 2020. Interface microstructure characteristics of friction-welded joint of titanium to stainless steel with interlayer. Transactions of the Indian Institute of Metals. 73(6), 1497-1501.

[3] Cheepu, M., Che, W.S., 2020. Influence of friction pressure on microstructure and joining phenomena of dissimilar joints. Transactions of the Indian Institute of Metals. 73(6), 1455-1460.

[4] Cheepu, M., Che, W.S., 2019. Friction welding of titanium to stainless steel using Al interlayer. Transactions of the Indian Institute of Metals. 72(6), 1563-1568.

[5] Kong, Y.S., Cheepu, M., Park, Y.W., 2020. Effect of heating time on thermomechanical behavior of friction-welded A105 bar to A312 pipe joints. Transactions of the Indian Institute of Metals. 73(6), 1433-1438.

[6] Muralimohan, C.H., Muthupandi, V., Sivaprasad, K., 2014. Properties of friction welding titanium-stainless steel joints with a nickel interlayer. Procedia Materials Science. 5, 1120-1129.

[7] Yoon, J.Y., Cheon, J., Kim, C., 2019. Characteristic Evaluation of Coaxial High-Frequency Induction Heating Hybrid Friction Stir Welding Process on High Strength Carbon Steel Sheets. Journal of Welding and Joining. 37(6), 585-590.

[8] Cheepu, M., Venkateswarlu, D., Rao, P.N., Muthupandi, V., Sivaprasad, K., Che, W.S., 2019. Microstructure characterization of superalloy 718 during dissimilar rotary friction welding. Materials Science Forum. 969, 211-217.

[9] Cheepu, M., Che, W.S., 2019. Effect of burn-off length on the properties of friction welded dissimilar steel bars. Journal of Welding and Joining. 37(1), 40-45.

[10] Cheepu, M., Muthupandi, V., Che, W.S., 2018. Improving mechanical properties of dissimilar material friction welds. Applied Mechanics and Materials. 877, 157-162.

[11] Muralimohan, C.H., Muthupandi, V., Sivaprasad, K., 2014. The influence of aluminium intermediate layer in dissimilar friction welds. International Journal of Materials Research. 105(4), 350-357.

[12] Cheepu, M., Muthupandi, V., Loganathan, S., 2012. Friction welding of titanium to 304 stainless steel with electroplated nickel interlayer. Materials Science Forum. 710, 620-625.

[13] Chandra, G.R., Venukumar, S., Cheepu, M., 2020, December. Influence of rotational speed on the dissimilar friction welding of heat-treated aluminum alloys. IOP Conference Series: Materials Science and Engineering. 998(1), 012070.

[14] Cheepu, M., Ashfaq, M., Muthupandi, V., 2017. A new approach for using interlayer and analysis of the friction welding of titanium to stainless steel. Transactions of the Indian Institute of Metals. 70(10), 2591-2600.

[15] Muralimohan, C.H., Ashfaq, M., Ashiri, R., Muthupandi, V., Sivaprasad, K., 2016. Analysis and characterization of the role of Ni interlayer in the friction welding of titanium and 304 austenitic stainless steel. Metallurgical and Materials Transactions A. 47(1), 347-359.

[16] Cheepu, M., Muthupandi, V., 2013. Friction welding of type 304 stainless steel to CP titanium using nickel interlayer. Advanced Materials Research. 794, 351-357.

[17] James, J.A., Sudhish, R., 2016. Study on effect of interlayer in friction welding for dissimilar steels: SS 304 and AISI 1040. Procedia Technology. 25, 1191-1198.

[18] Muralimohan, C.H., Haribabu, S., Reddy, Y.H., Muthupandi, V., Sivaprasad, K., 2014. Evaluation of microstructures and mechanical properties of dissimilar materials by friction welding. Procedia Materials Science. 5, 1107-1113.

[19] Cheepu, M., Che, W.S., 2019. Characterization of microstructure and interface reactions in friction welded bimetallic joints of titanium to 304 stainless steel using nickel interlayer. Transactions of the Indian Institute of Metals. 72(6), 1597-1601.

[20] Cheepu, M., Che, W.S., 2020. Characterization of interfacial microstructure in friction welds between Inconel 718 and SM45C steel. Transactions of the Indian Institute of Metals. 73(6), 1597-1571.

[21] Kong, Y.S., Park, Y.W., 2019. Optimization of PWHT on Dissimilar Friction Welding for Piping Material of A105 to A312. Journal of Welding and Joining. 37(2), 60-65.

[22] Aali, M., 2020. Investigation of Spindle Rotation Rate Effects on the Mechanical Behavior of Friction Stir Welded Ti 4Al 2V Alloy. Journal of Welding and Joining. 38(1), 81-91.

[23] Muhammad, W., Husain, W., Tauqir, A., Wadood, A., 2020. Optimization of Friction Stir Welding Parameters of AA2014-T6 Alloy using Taguchi Statistical Approach. Journal of Welding and Joining. 38(5), 494.

[24] Kim, J.H., Kim, N.Y., Kong, Y.S., Park, N.K., 2019. Microstructure and Mechanical Properties of Friction-Welded Alloy 718 and SNCRW Stainless Steel after Post-Weld Heat-Treatment. Journal of Welding and Joining. 37(4), 313-317.

[25] Kong, Y.S., Cheepu, M., Lee, J.K., 2021. Evaluation of the mechanical properties of Inconel 718 to SCM 440 dissimilar friction welding through real-time

monitoring of the acoustic emission system. Proceedings of the Institution of Mechanical Engineers, Part L: Journal of Materials: Design and Applications. pp.1464420721993838.

[26] Cheepu, M., Kumar Reddy, Y.A., Indumathi, S., Venkateswarlu, D., 2021. Laser welding of dissimilar alloys between high tensile steel and Inconel alloy for high temperature applications. Advances in Materials and Processing Technologies. pp. 1-12.

[27] Nadikudi, B.K.B., 2019. Behaviour of friction stir dissimilar welded blanks and the role of different tool pin profiles. Journal of Metallic Material Research. 2(2), 15-19.

[28] Cheepu, M., Venkateswarlu, D., Rao, P.N., Kumaran, S.S., Srinivasan, N., 2019. Effect of process parameters and heat input on weld bead geometry of laser welded titanium Ti-6Al-4V alloy. Materials Science Forum. 969, 613-618.

[29] Kong, Y.S., Cheepu, M., Kim, D.G., 2020. Microstructure and Mechanical Properties of Friction-Welded and Post-Heat-Treated Inconel 718. Transactions of the Indian Institute of Metals. 73(6), 1449-1453.

[30] Cheepu, M., Susila, P., 2020. Growth rate of intermetallics in aluminum to copper dissimilar welding. Transactions of the Indian Institute of Metals. 73(6), 1509-1514.

[31] Cheepu, M., Muthupandi, V., Che, W.S., 2019. Interface microstructural characterization of titanium to stainless steel dissimilar friction welds. In TMS 2019 148th Annual Meeting & Exhibition Supplemental Proceedings. Springer, Cham., pp. 259-268.

[32] Muralimohan, C.H., Haribabu, S., Reddy, Y.H., Muthupandi, V., Sivaprasad, K., 2015. Joining of AISI 1040 steel to 6082-T6 aluminium alloy by friction welding. Journal of Advances in Mechanical Engineering and Science. 1(1), 57-64.

[33] Jabbar Hassan, A., Boukharouba, T., Miroud, D., 2020. Friction welding of AISI 304: effect of friction time on micro-structure, micro-hardness and tension-compression properties. Acta Metallurgica Slovaca. 26(3), 78-83.

Journal of Metallic Material Research
https://ojs.bilpublishing.com/index.php/jmmr

ARTICLE

Influence of Nanoparticle Shapes of Boehmite Alumina on the Thermal Performance of a Straight Microchannel Printed Circuit Heat Exchanger

Élcio Nogueira*

Department of Mechanic and Energy, State University of Rio de Janeiro, Brazil

ARTICLE INFO

Article history
Received: 19 January 2022
Accepted: 11 February 2022
Published Online: 18 February 2022

Keywords:
Shapes of nanoparticles
Boehmite alumina
Straight microchannel
Printed circuit heat exchanger (PCHE)
Al_2O_3

ABSTRACT

The efficiency and irreversibility defined based on the second law of thermodynamics provide a new path for heat exchangers design and make performance analysis more straightforward and elegant. The second law of thermodynamics is applied in a Straight Microchannel Printed Circuit heat exchanger to determine the thermal performance of different shapes of Boehmite Alumina compared to Al_2O_3 aluminum oxide. The various forms of non-spherical Boehmite Alumina are characterized dynamically and thermodynamically through dynamic viscosity and thermal conductivity, using empirical coefficients. The non-spherical shape includes platelet, cylindrical, blades, and bricks forms. Graphical results are presented for thermal efficiency, thermal irreversibility, heat transfer rate, and nanofluid exit temperature. The non-spherical shapes of Boehmite Alumina show different thermal characteristics concerning the spherical shape when there are variations in fluid flow rates and the nanoparticles fraction. Furthermore, it was theoretically demonstrated that non-spherical particles have higher heat transfer rates than spherical particles, emphasizing platelets and cylindrical shapes for the low volume fraction of nanoparticles and bricks and blades for high volume fraction.

1. Introduction

This work aims to theoretically analyze the thermal performance of a Straight Microchannel Printed Circuit heat exchanger when using non-spherical forms of Boehmite Alumina, compared to the Al_2O_3 aluminum oxide. The methodology is based on thermal efficiency and effectiveness. Efficiency, in this case, is a function of a single dimensionless parameter called the fin analogy, which is like the efficiency of a fin constant-area with an insulated tip, and applies to parallel-flow, counter-flow, and crossflow heat exchangers.

A review of the second law of thermodynamics regarding heat and mass transfer was published during the 1980s, where the fundamental mechanisms responsible for entropy generation were analyzed. It demonstrated how to balance the irreversibility of heat transfer versus the irreversibility of fluid flow and how the reduction in

---

*Corresponding Author:
Élcio Nogueira,
Department of Mechanic and Energy, State University of Rio de Janeiro, Brazil;
Email: elcionogueira@hotmail.com

DOI: https://doi.org/10.30564/jmmr.v5i1.4364

irreversibility at the component level affects the entire system. Effectiveness, defined based on the second law, provides a new way to design and analyze heat exchangers, as thermal performance is usually measured by the ratio of current heat transfer rate to ideal transfer rate. However, it does not provide information about efficiency and irreversibility, which measure the degree of entropy generation in a physical system [1-3]. Nogueira, E. applies the second thermodynamics law to analyze and design heat exchangers. For example, he uses this new way for studying a shell and tube and shell and helical coil tube heat exchangers [4,5].

Lei Chai and Savvas A. Tassou [6] state that printed circuit heat exchangers (PCHEs) are a promising technology due to their highly compact construction. They enable high heat transfer coefficients, withstand high pressures, and operate over a wide temperature range. They analyze relatively new heat exchangers and projects that are still in development. They argue that PCHEs are well established in the petrochemical industry. However, they say, it takes a lot of effort to increase the attractiveness of a market that includes a vast range of applications. They mention the need to develop empirical correlations better to predict the performance of the heat exchanger in general.

A printed circuit heat exchanger (PCHE) made of thin diffusion bonded metal plates is lightweight, has high structural strength, enables microchannel processing on the metal surface, is easy to produce, has high reliability and economic efficiency. Moreover, there is almost no thermal resistance between the microchannels to achieve excellent thermal performance. Thermal performance tests were performed for a PCHE for Reynolds numbers in 100-850. It was found that the heat transfer rate increased with increasing Reynolds number in all experiments. Furthermore, empirical correlations were obtained for the heat transfer coefficient for PCHE applications in the analyzed Reynolds number range [7].

Salah Almurtaji et al. [8] argue that heat exchangers are essential in everyday applications. For example, they are used in land vehicles, oil refineries, air conditioning, and water heating. Their review presents state of the art in heat exchanger technology and the use of nanofluids in current devices. In addition, they discuss the development of nanofluids and their influence on the thermo-hydraulic performance of heat exchangers and emphasize the important role of nanofluids in the thermal performance of current heat exchangers.

Iman Zahmatkesh et al. [9] indicate a growing number of published articles related to nanofluids in thermal systems, but there is no specific review on the forms of nanoparticles. The study carried out indicates a lack of definitive conclusion on how the shape of nanoparticles affects the performance of thermal systems. They report that the platelet-shaped nanoparticle enables the highest heat transfer rate in natural and forced convection. However, the best performance occurs for a lamina-shaped nanoparticle in the mixed convection regime. They conclude that studies are needed to determine the effective contribution of nanoparticle forms to the thermal performance of energy systems.

Mostafa Monfared et al. [10] Study the effects of the shape of nanoparticles on the entropy generation characteristics in a horizontal double tube heat exchanger. Nanofluids examined include cylindrical, brick, blade, platelet, and spherical nanoparticles. The effects produced by the concentrations of nanoparticles and the different forms of nanoparticles on the rates of thermal entropy generation were investigated numerically. Results indicate that nanofluid containing spherical and platelet-shaped nanoparticles represent, respectively, the maximum and minimum thermal generation rates. Furthermore, it was observed that the rate of thermal entropy generation decreases with an increase in the concentration of nanoparticles, except for those with a spherical shape.

Behrouz Raeia and Sayyed Mohsen Peyghambarzadeh [11] experimentally determined the heat transfer coefficient and thermal efficiency of γ-Al_2O_3/water nanofluids in a double-tube heat exchanger. Nanoparticles dispersed in distilled water range from 0.05% to 0.15% volume fractions. Fluid flows, in turbulent flow regime, show variations in the Reynolds number between 18,000 and 40,000. The addition of nanoparticles to the base fluid allowed an increase in heat transfer of up to 16%. The thermal performance factor reaches 1.11 for nanoparticles concentration equal to 0.15 vol.% and Reynolds number equal to 18,000.

Xiao Feng Zhou and L. Gao [12] estimates the effective thermal conductivity in non-spherical solid particle nanofluids through the differential effective medium theory, considering the interfacial thermal resistance between the solid particles and the host liquids. There was a high increase in the effective thermal conductivity of non-spherical nanoparticles, and the increase in interfacial thermal resistance results in appreciable degradation in the rise in thermal conductivity. The theoretical results agree with experimental data on nanofluids and show the non-linear dependence of the effective thermal conductivity with the volume fractions of non-spherical nanoparticles.

Elena V. Timofeeva et al. [13] investigated experimentally and theoretically modeling the thermal conductivity and viscosity in a fluid consisting of equal volumes of ethylene glycol and water analyzed. They note that the increase in effective thermal conductivity is greatly diminished by interfacial effects proportional to the total surface area of the nanoparticles and that the surface charge of nanoparticles plays a vital role in viscosity. They demonstrate that adjusting the pH of the nanofluid and reducing the viscosity of the nanofluid without significantly affecting the thermal conductivity. The efficiency of nanofluids the ratio between thermal conductivity and viscosity in both laminar and turbulent flow regimes are evaluated.

2. Methodology

The second law of thermodynamics is applied in a Straight Microchannel Printed Circuit heat exchanger to determine the thermal performance of different forms of Boehmite Alumina compared to Al_2O_3 aluminum oxide. The heat exchanger is represented in Figure 1 below [7].

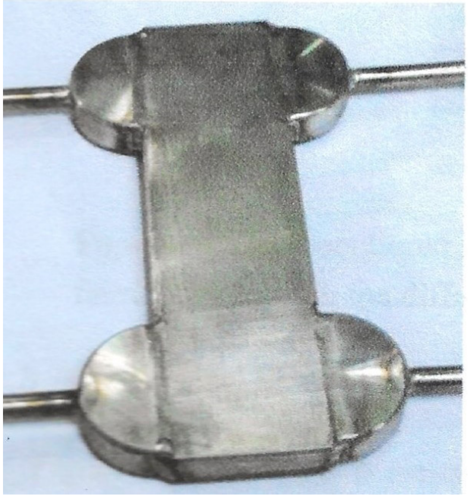

Figure 1. Straight Microchannel Printed Circuit Heat Exchanger [7]

The various forms of non-spherical Boehmite are characterized dynamically and thermodynamically through dynamic viscosity and thermal conductivity, Equations 6 and 9, using empirical coefficients, presented by Mostafa Monfared et al. [8]. Table 1 gives the properties of hot (Water), cold (Ethylene Glycol) fluids, and nanoparticles of Al_2O_3 and spherical Boehmite Alumina. The non-spherical shape of Boehmite includes platelet, cylindrical, blades, and bricks forms. Table 2 presents the coefficients used to determine the dynamic viscosity and thermal conductivity for different shapes of Boehmite Alumina.

$$Dh_c = \frac{4Ac_c Lf_c}{As_c} \tag{1}$$

Dh_c is the hydraulic diameter, Ac_c=$42.2\times10^{-6}\,\mathrm{m}^2$ Lf_c= $137\times10^{-3}\,\mathrm{m}$, Lf_c=$137\times10^{-3}\,\mathrm{m}$ is the length of the cold flow stream, As_c=$34.716\times10^{-3}\,\mathrm{m}^2$ is the total cold area of the heat transfer area.

$$Dh_h = Dh_c \tag{2}$$

$$Lf_h = \frac{Dh_h As_h}{4Ac_h} \tag{3}$$

Lf_h is the length of the hot flow stream, $As_h = 26.037\times 10^{-3}\,\mathrm{m}^2$ is the total hot area of heat transfer area.

The properties of the nanofluids are:

$$\rho_{nano} = \rho_{Particle}\phi + (1-\Phi)\rho_c \tag{4}$$

$$\mu_{nano} = \frac{\mu_c}{(1-\phi)^{2.5}} \tag{5}$$

$$\mu_{nano} = \mu_c(1 + A_1\phi + A_2\phi^2) \quad \textit{for non-spherical shape} \tag{6}$$

$$Cp_{nano} = \frac{Cp_{Particle}\rho_{Particle}\phi + (1-\phi)\rho_C}{\rho_{nano}} \tag{7}$$

$$k_{nano} = [\frac{[k_{Particle} + 2k_c + 2(k_{Particle} - k_c)(1-0.1)^3\phi]}{[k_{Particle} + 2k_c + 2(k_{Particle} - k_c)(1-0.1)^2\phi]}]k_c \tag{8}$$

$$k_{nano} = k_c(1 + C_k\phi) \quad \textit{for non-spherical shape} \tag{9}$$

$$\nu_{nano} = \frac{\mu_{nano}}{\rho_{nano}} \tag{10}$$

$$\alpha_{nano} = \frac{k_{nano}}{\rho_{nano}Cp_{nano}} \tag{11}$$

$$\Pr_{nano} = \frac{\nu_{nano}}{\alpha_{nano}} \tag{12}$$

$$\mu_W = \frac{\mu_{nano} + \mu_h}{2} \tag{13}$$

μ_w is the assumed value for the fluid viscosity in the channel wall.

Table 1. Hot (Water), cold (Ethylene Glycol 50%) fluids and nanoparticles properties

	ρ kg/m^3	k W/ (m K)	Cp J/(kg K)	μ kg/(m s)	ν m/s^2	α m/s^2	Pr
Hot	**994**	**0.623**	**4178**	**0.72×10^{-3}**	**7.24×10^{-7}**	**1.5×10^{-7}**	**4.83**
Cold	**1067.5**	**0.3799**	**3300**	**3.39×10^{-3}**	**2.4045×10^{-5}**	**1.08×10^{-7}**	**0.02**
Al_2O_3	**3950**	**31.92**	**873.34**	**-**	-	**9.25×10^{-6}**	**-**
B Alumina	**3050**	**30**	**618.3**	**-**	-	**1.59×10^{-5}**	**-**

Table 2. Coefficients defined in Equation 6 and Equation 9 for inclusion of nanoparticle shape in dynamic viscosity and thermal conductivity [8]

Type	C_k	A_1	A_2
Platelets	2.61	37.1	612.6
Blades	2.74	14.6	123.3
Cylindrical	3.95	13.5	904.4
Bricks	3.37	1.9	471.4

$$h_{nano} = 0.1706\ 6^{0.44}\ \mathrm{Re}_{nano}{}^{0.324}\ \mathrm{Pr}_{nano}{}^{1/3}(\frac{\mu_{nano}}{\mu_W})^{0.14}(\frac{k_{nano}}{Dh_c}) \qquad (14)$$

$$h_h = 0.1729\ 5^{0.44}\ \mathrm{Re}_h{}^{0.324}\ \mathrm{Pr}_h{}^{1/3}(\frac{\mu_h}{\mu_W})^{0.14}(\frac{k_h}{Dh_h}) \qquad (15)$$

The heat transfer coefficients of both fluids, cold h_{nano} and hot h_h, were obtained by regression fit [7].

$$A_{Med} = \frac{As_h + As_c}{2} \qquad (16)$$

The overall heat transfer coefficient is given by:

$$U_O A = \frac{1}{\frac{1}{h_h As_h} + \frac{1}{h_{nano} As_C} + \frac{L}{k_{Metal} A_{Med}}} \qquad (17)$$

$k_{Metal} = 16.2\mathrm{W/(mK)}$ is the thermal conductivity of the heat transfer plate and $L = 0.4 \times 10^{-3}\mathrm{m}$ is the gap between the cold and hot channels.

$$\dot{m}_h = \frac{\mathrm{Re}_h\ \mu_h Ac_h}{Dh_h} \qquad (18)$$

$$\dot{m}_{nano} = \frac{\mathrm{Re}_{nano}\ \mu_{nano} Ac_c}{Dh_c} \qquad (19)$$

$\dot{m}_h$ and $\dot{m}_{nano}$ are the mass flow rates of the hot and cold fluid, respectively.

$$C_h \doteq m' Cp_h \qquad (20)$$

$$C_{nano} \doteq m' Cp_{nano} \qquad (21)$$

C_h and C_{nano} are the heat capacity of the hot and cold fluid, respectively.

$$C^* = \frac{C_{\min}}{C_{max}} \qquad (22)$$

Where $C_{\min}$ is the minimum between and C_{nano}.

$$NTU = \frac{U_O A}{C_{\min}} \qquad (23)$$

NTU are the number of thermal units associated with the heat exchanger.

$$Fa = \frac{NTU(1 - C^*)}{2} \qquad (24)$$

Fa is the fin analogy for a counter-flow heat exchanger [2,3,14].

$$\eta_T = \frac{\tanh(Fa)}{Fa} \qquad (25)$$

η_T is the thermal efficiency.

$$\varepsilon_T = \frac{1}{\frac{1}{\eta_T NTU} + \frac{1 + C^*}{2}} \qquad (26)$$

ε_T is the thermal effectiveness.

$$\dot{Q}_{Max} = (Th_i - Tc_i) C_{\min} \qquad (27)$$

$\dot{Q}_{Max}$ is the theoretically possible maximum of the heat transfer rate for the situation in analysis.

$$\dot{Q} = \frac{(Th_i - Tc_i) C_{\min}}{\frac{1}{\eta_T NTU} + \frac{1 + C^*}{2}} \qquad (28)$$

$\dot{Q}$ is the actual heat transfer rate.

The outlet temperatures for both fluids, T_{h0} and T_{c0}, are given by:

$$Th_o = Th_i - \frac{Q'}{m' Cp_h} \qquad (29)$$

$$Tc_o = Tc_i + \frac{Q'}{m' Cp_{nano}} \qquad (30)$$

$$\sigma_T = (\frac{C_h}{C_{\min}}) \ln(\frac{Th_o}{Th_i}) + (\frac{C_{nano)}}{C_{\min}}) \ln(\frac{Tc_o}{Tc_i}) \qquad (31)$$

σ_T is the thermal irreversibility for the heat exchanger.

3. Results and Discussion

Graphical results related to nanofluid properties, emphasizing momentum diffusivity and thermal diffusivity, are shown in Figures 1 to 4. Figures 6 to 10 show results for heat transfer rate and associated quantities for $\mathrm{Re_h}$=800 and $\mathrm{Re_c}$=200, and Figures 11 to 15 for $\mathrm{Re_h}$=800 and $\mathrm{Re_c}$=600. Figures 16 and 17 show the hot fluid exit temperature with Reynolds numbers ranging from 200 to 400 for hot fluid and cold nanofluid.

Figure 1 presents results for dynamic viscosity for a variation of volume fraction between 0 and 15%. The highlighted figure represents the kinematic viscosity, representing the quantity of motion and having quantitative similarity with the dynamic viscosity. The similarity demonstrates that dynamic viscosity is the main factor in determining the momentum, with specific mass (density) influencing only in the order of magnitude. Non-spherical nanoparticles significantly increase the momentum of the nanofluid, with emphasis on platelets, cylindrical, and blades. The spherical nanoparticles, Al_2O_3 aluminum oxide, and Boehmite Alumina present lower values for the momentum for the entire range of volume fraction analyzed and showed similar graphic results, as they have very identical numerical thermodynamic properties (Table 1).

Figure 2 presents results for thermal conductivity for a variation of volume fraction between 0 and 15%. Non-spherical Cylindrical Boehmite Alumina has a higher thermal conductivity value than spherical nanoparticles, and Non-spherical Platelets and Blades have lower values. On the other hand, non-spherical Bricks have values very close to spherical particles for a high volume fraction of nanoparticles.

Figure 3 represents the thermal diffusivity and has quantitative similarity with the thermal conductivity. Figure 4 presents results for specific heat for a variety of volume fractions between 0 and 15%. The similarity demonstrates that thermal conductivity is the main factor in determining thermal diffusivity, with specific mass (density) and specific heat influencing only in the order of magnitude.

Figure 5 presents results for thermal capacity for cold and hot fluids as a function of the Reynolds number for a volume fraction equal to 0.05. The thermal capacity increases with increasing Reynolds number for all forms of nanoparticles. The highest values are associated with non-spherical platelets and cylindrical nanoparticles and the lowest in the hot fluid. This result obtained for the hot fluid is significant because the maximum heat transfer rate is theoretically possible, is associated with the lowest thermal capacity between the fluids, and serves as a reference for current heat transfer rates. As the thermal capacity represents the amount of energy in the form of heat absorbed by the medium, by the different temperature, the presented results will reflect on the heat transfer rate between the fluids.

Figure 6 presents results for heat transfer rate as a function of Reynolds number for volume fraction $\Phi=0.15$. For smaller values of Reynolds numbers, the heat transfer rate significantly approaches the maximum possible, preliminarily indicating that, in this case, the efficiency is relatively low and the irreversibility high. However, the inverse is expected for high Reynolds number values, as the current heat transfer rate is relatively low compared to the maximum possible. In the highlighted figure, the heat transfer rate is presented for the upper range of Reynolds number to better note the dispersion between the results related to the nanoparticle shapes.

Figure 7 presents results of heat transfer rate versus volume fraction for the nanoparticles, with $Re_h=800$ and $Re_c=200$ as parameters. For smaller volume fractions of the nanoparticles, it is observed that the platelet and cylindrical particles have a higher heat transfer rate. However, the brick-shaped particles and blade surpass the two previously mentioned heat transfer rates for high volume fraction values. In the entire range of volume fractions analyzed, the lowest values for heat transfer rate are associated with spherical particles.

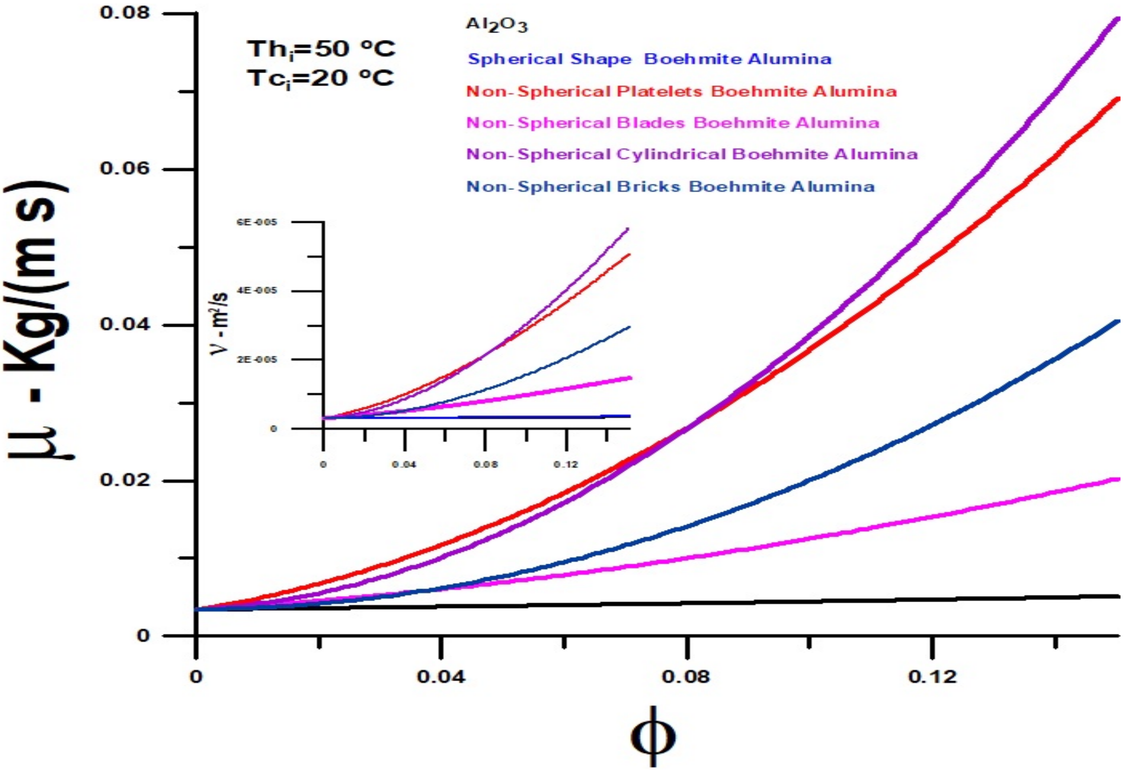

Figure 1. Dynamic and kinematic viscosities versus nanoparticle volume fraction

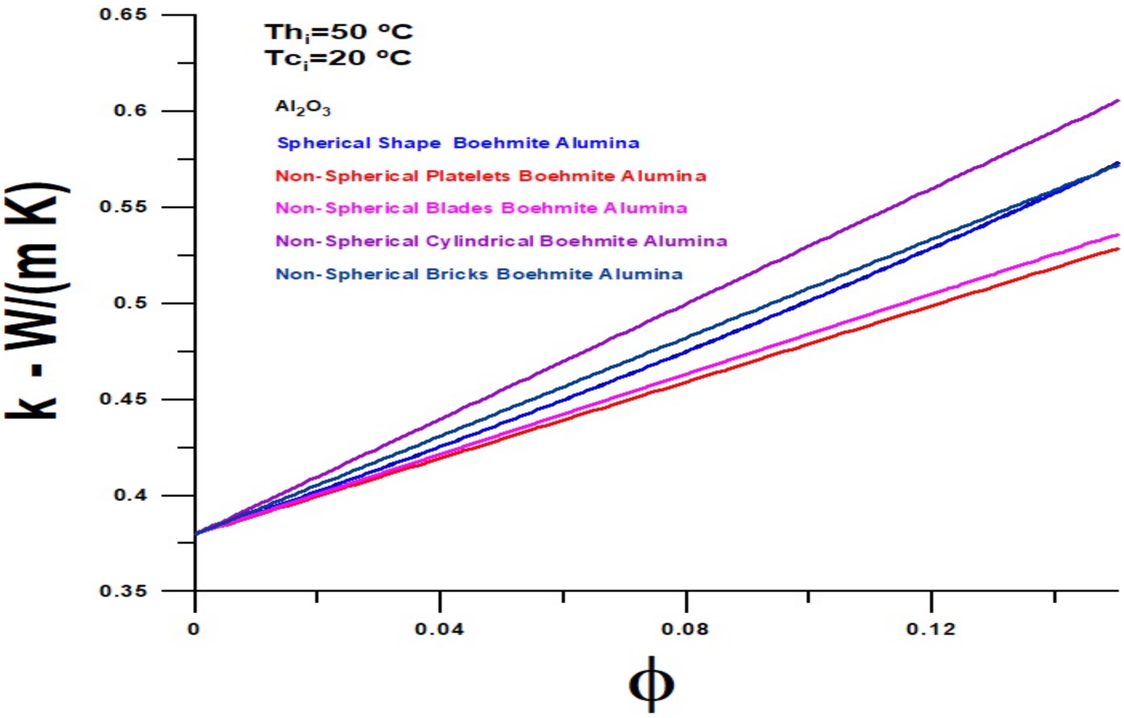

Figure 2. Thermal conductivity versus nanoparticle volume fraction

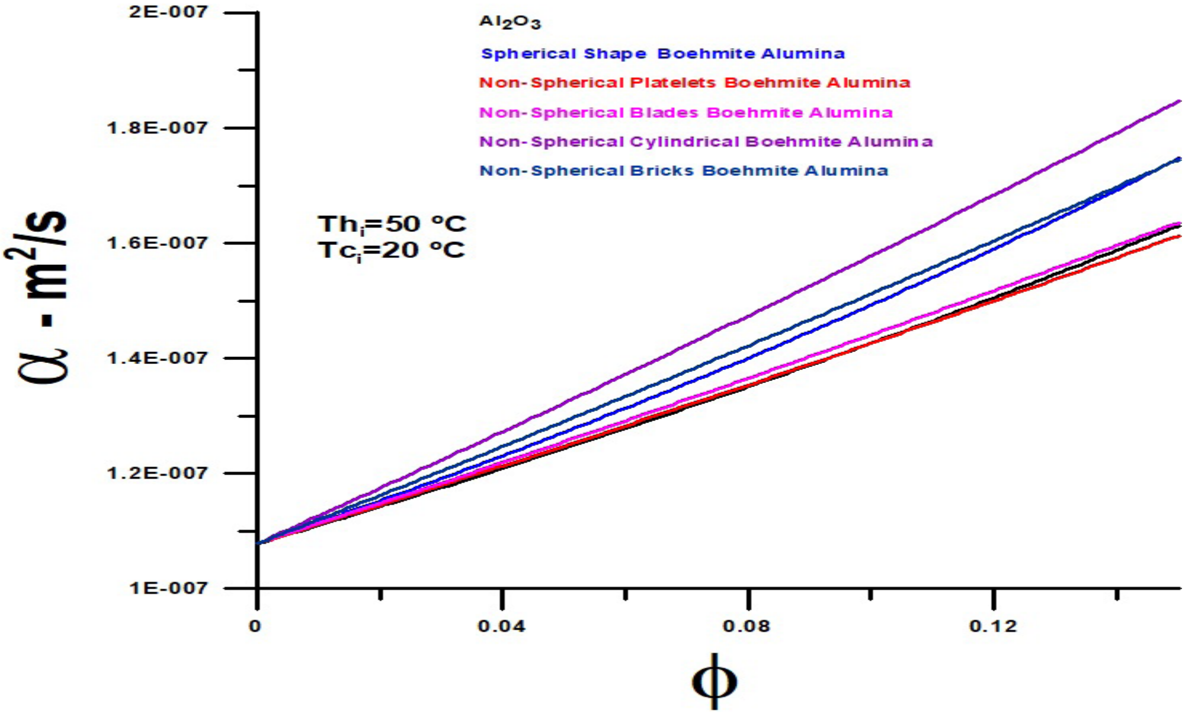

Figure 3. Thermal diffusivity versus nanoparticle volume fraction

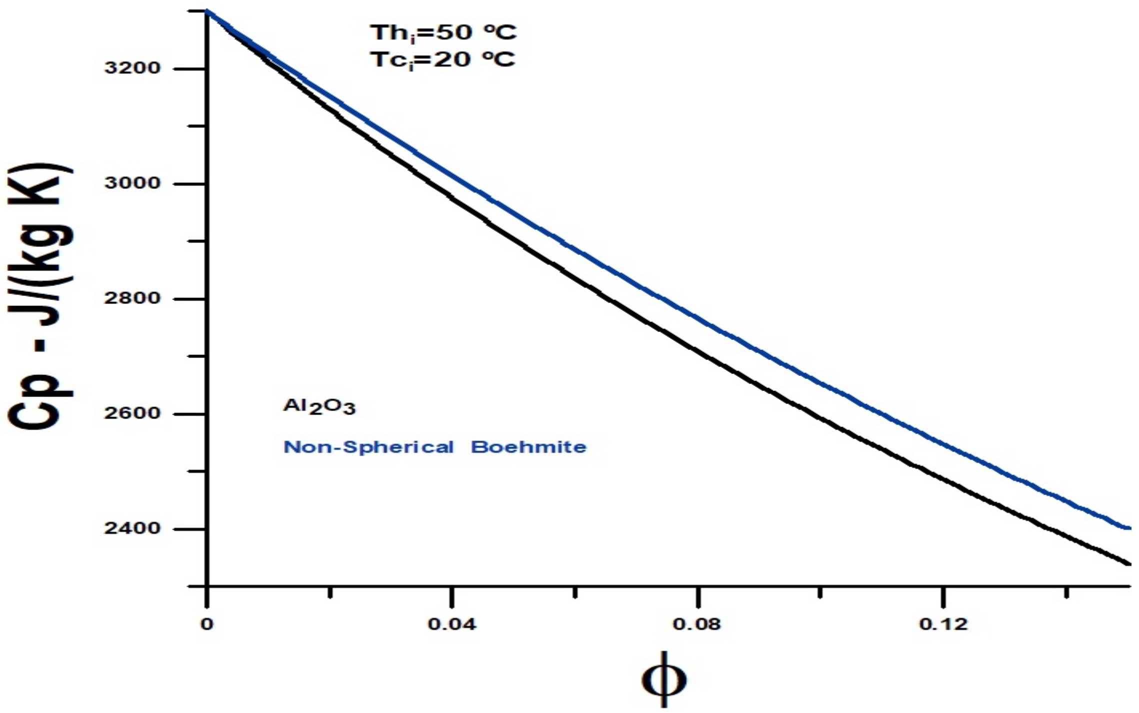

Figure 4. Specific heat and thermal diffusivity versus nanoparticle volume fraction

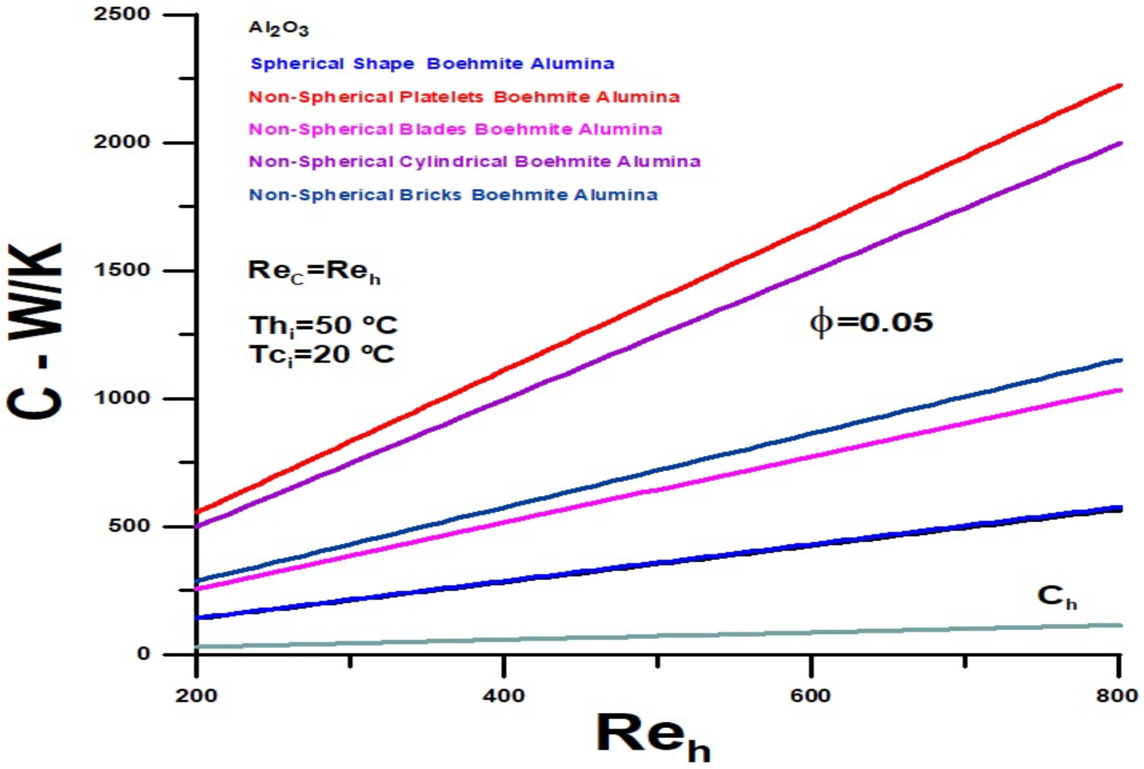

Figure 5. Thermal capacity versus Reynolds number

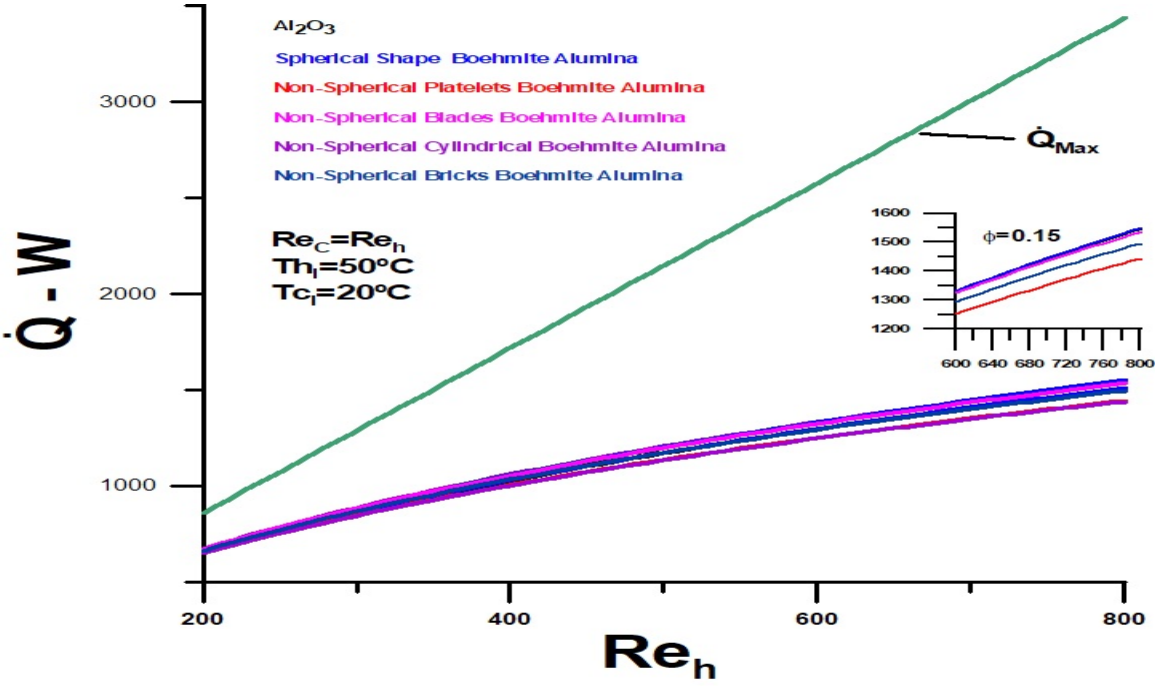

Figure 6. Actual and maximum heat transfer rate versus Reynolds number

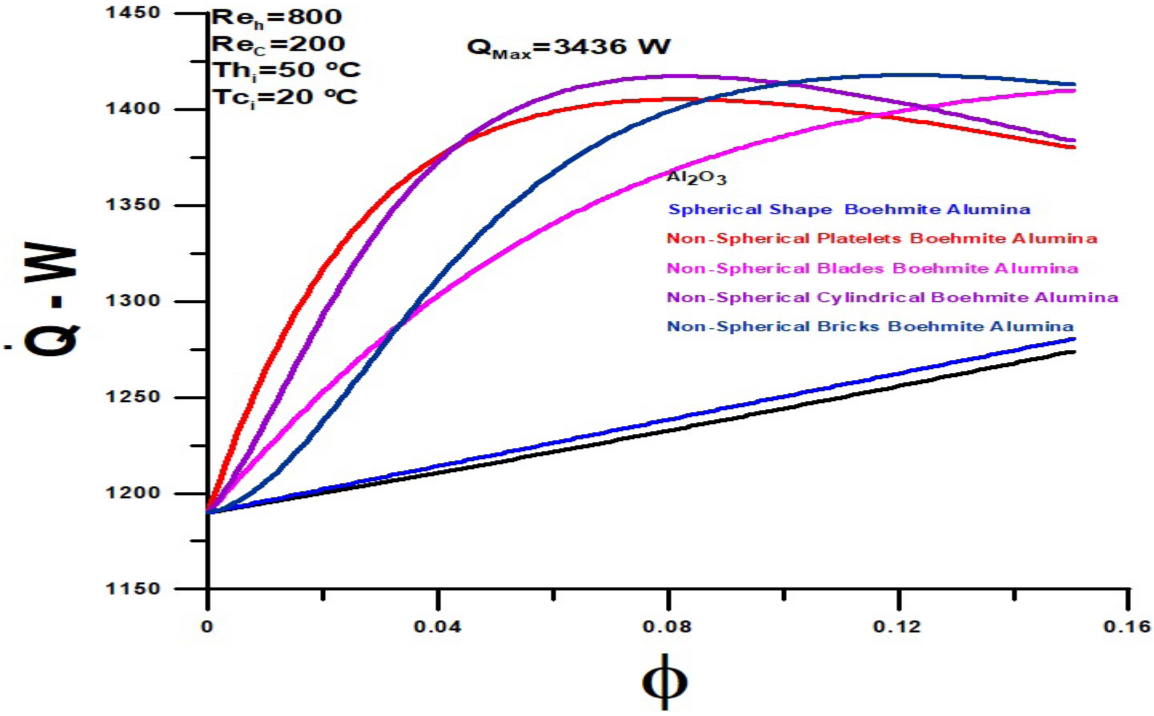

Figure 7. Heat transfer rate versus volume fraction of nanoparticles Re_h=800 and Re_c=200

Figure 8 shows the heat transfer rate as a function of the Prandtl number. The highlighted figure presents Prandtl number versus volume fraction. The Prandtl number grows with the volume fraction similar to that obtained for the momentum diffusivity, and the highest values are obtained for the non-spherical cylindrical and platelet shapes in the entire volume fraction range. The relevant fact is that Prandtl decreases with the increase in volume fraction for the spherical nanoparticles. The central figure, heat transfer rate versus Prandtl, highlights this fact, demonstrating that the Prandtl number increases, the heat transfer rate decreases for spherical nanoparticles, which have relatively low values for the Prandtl number. The highest Prandtl number values are obtained for non-spherical cylindrical and platelet nanoparticles, which have a slightly lower thermal performance than non-spherical blade and Brick type nanoparticles. Non-spherical particles have high values for heat transfer rates regarding spherical particles. It is noteworthy that the heat transfer rate goes through a maximum value with an increase in the Prandtl number, with the rise in the fraction in volume. Non-spherical Blade nanoparticles did not reach the maximum value for heat transfer for the maximum volume fraction under analysis equal to Φ=0.15, and, in this case, it is possible to increase the volume fraction until the maximum heat transfer rate.

Figure 9 presents thermal irreversibility results, representing the generation of entropy, as a function of the volume fraction of the nanoparticles for Reh=800 and Rec=200. Values for thermal irreversibility are relatively low concerning total entropy, which considers the portion of entropy generation associated with the viscosity of the medium. Entropy generation grows with the volume fraction for all nanoparticles and is relatively high for non-spherical nanoparticles compared to entropy generation for spherical particles. The nanoparticle shapes affect the interaction between the base fluid and the nanoparticles, creating greater irreversibility. There is a clear relationship between the heat transfer rate exchanged between fluids and irreversibility (Figure 7). The greater irreversibility is achieved for non-spherical cylindrical and platelet nanoparticles. The entropy generation rate did not reach the maximum for the non-spherical nanoparticle Blade, within the volume fraction range equal to 0.0 and 0.15. The maximum entropy generation for the non-spherical nanoparticle Bricks is reached near the equal volume fraction to 0.15.

Figure 10 presents results for thermal efficiency as a function of the volume fraction of the nanoparticles for Re_h=800 and Re_c=200. Efficiency is low where irreversibility is high, when heat transfer rate is high, or when there is high entropy generation. In this sense, Figures 8

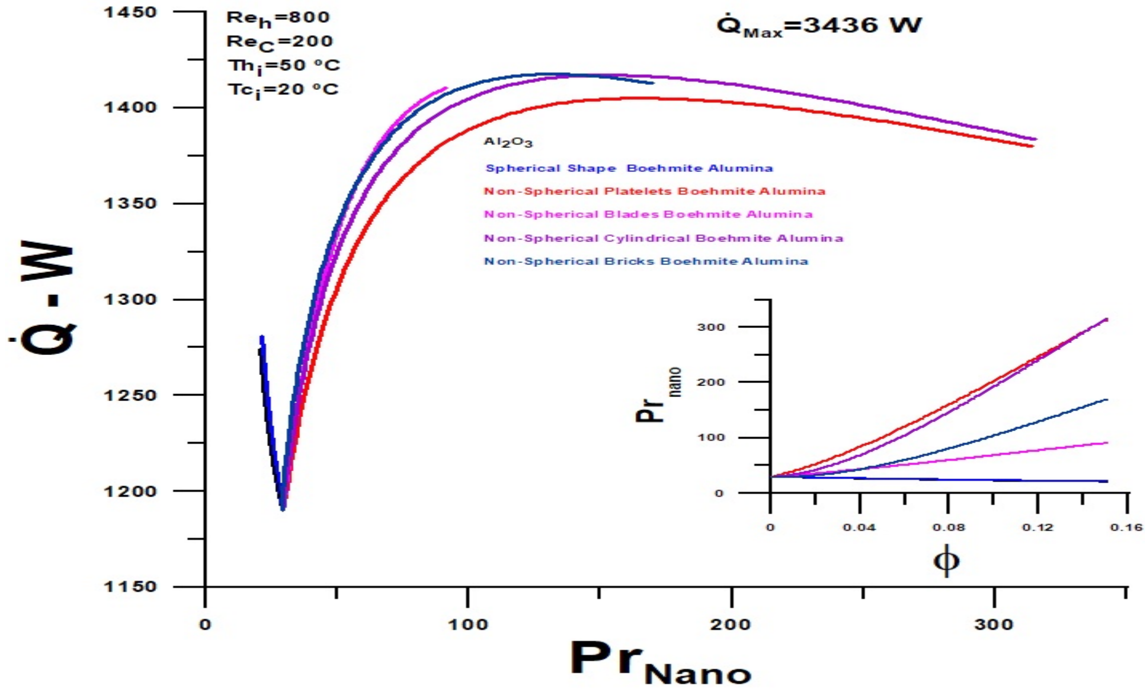

Figure 8. Heat transfer rate versus Prandtl number and Prandtl number versus volume fraction Re_h=800 and Re_c=200

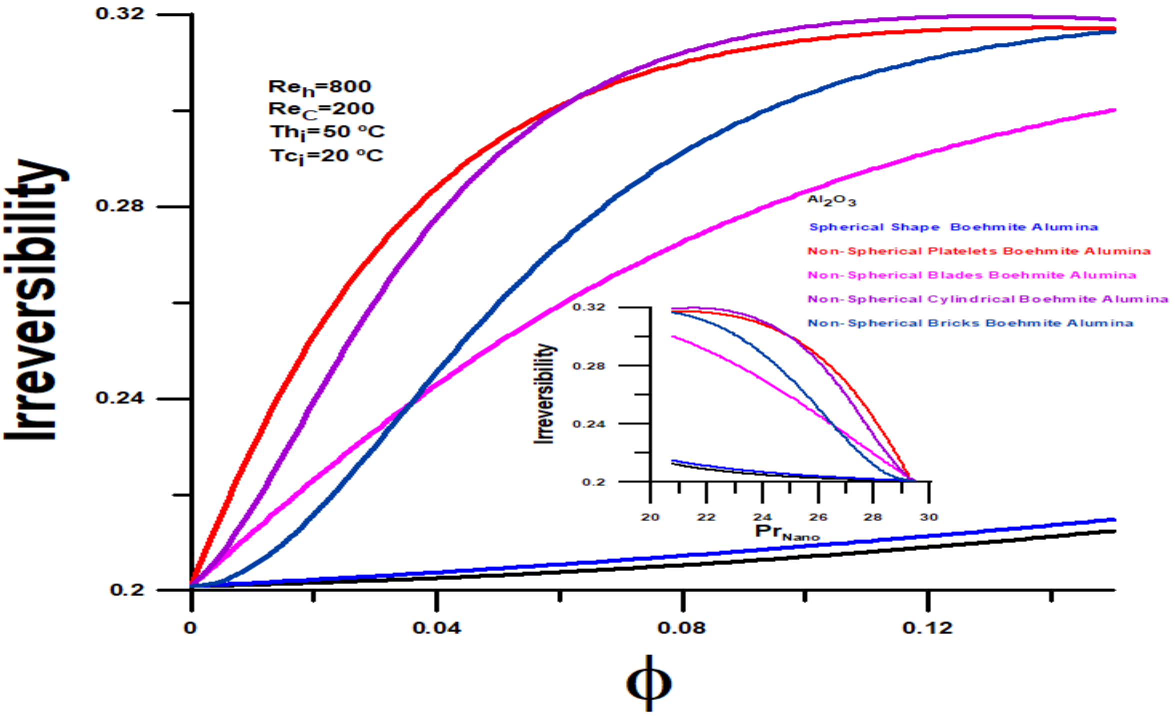

Figure 9. Irreversibility versus volume fraction of nanoparticles and Prandtl number Re_h=800 and Re_c=200

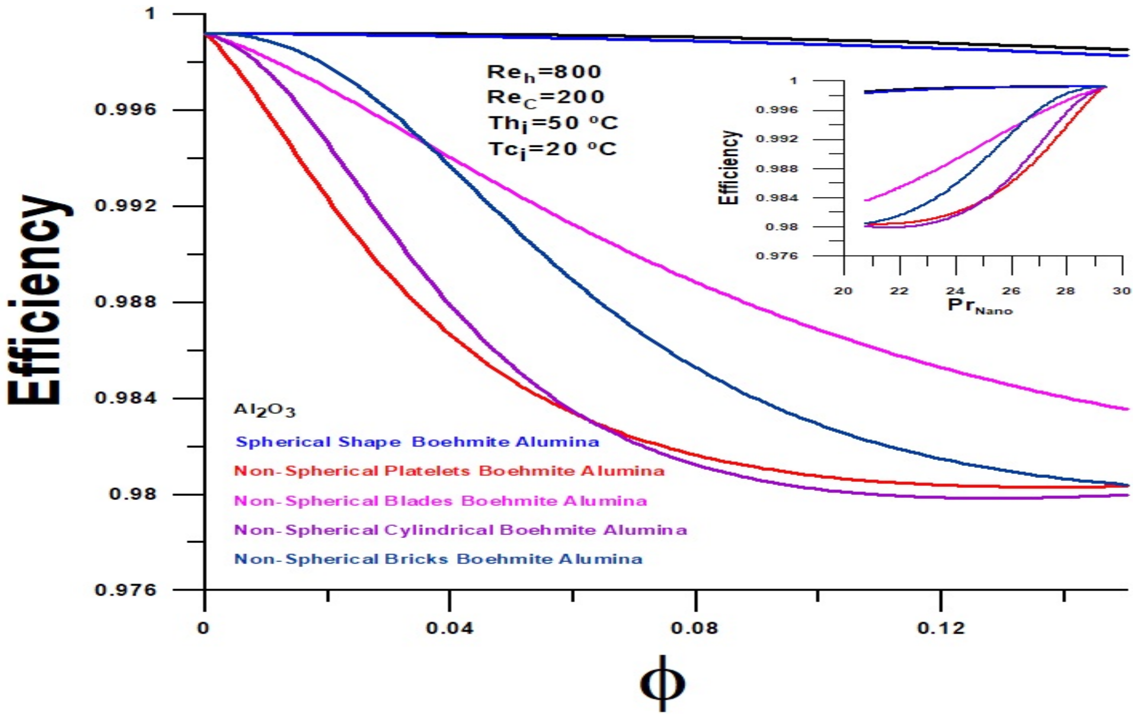

Figure 10. Efficiency versus volume fraction of nanoparticles and Prandtl number Re_h=800 and Re_c=200

and 9 complements each other and corroborate the results obtained for the heat transfer rate observed for the nanofluid through Figures 6 and 7.

Figure 11 shows the hot fluid outlet temperature as a function of the volume fraction of the nanoparticles and complements the information already obtained for Re_h=800 and Re_c=200. The lowest outlet temperature occurs when irreversibility is high or greater heat exchange between the media, corresponding to non-spherical cylindrical and brick nanoparticles for different volume fractions. Cylindrical nanoparticles reach a lower temperature in a volume fraction equal to 0.8 and the brick nanoparticle close to 0.12. For blade nanoparticles, a lower output temperature can be reached for a volume fraction greater than 0.15.

Figure 12 presents results of heat transfer rate versus volume fraction for the nanoparticles, with Re_h=800 and Re_c=600 as parameters. The absolute values of the heat transfer rate are significantly higher concerning the condition Re_h=800 and Re_c=200. For smaller volume fractions of nanoparticles, platelets and cylindrical particles increase the heat transfer rate and higher value. In these cases, when the volume fraction increases, they go through a maximum heat transfer rate between 0.4 and 0.8 and decrease until the heat transfer rate is below the value obtained for the spherical nanoparticles for volume fractions above 0.10. For volume fractions above 0.8, Blades and Bricks nanoparticles show better thermal performance than others. The non-spherical blade nanoparticle has a higher heat transfer rate than spherical nanoparticles in the entire range of analyzed volume fraction.

Figure 13 shows heat transfer rate versus Prandtl number, and highlighted figure presents Prandtl number versus volume fraction, for Re_h= 800 and Re_c=600. The Prandtl number decreases with increasing volume fraction for spherical nanoparticles. Heat transfer rate versus Prandtl demonstrates that when the Prandtl number rises, the heat transfer rate decreases for spherical nanoparticles, which have relatively low values for the Prandtl number. The highest Prandtl number values are obtained for cylindrical and non-spherical platelet nanoparticles, with slightly lower thermal performance than the non-spherical blade and Brick-type nanoparticles. Non-spherical particles have high values for heat transfer rates relative to spherical particles. The heat transfer rate goes through a maximum value as the Prandtl number increases, that is, as the volume fraction increases for all non-spherical nanoparticles. All non-spherical nanoparticles have a maximum value for the heat transfer rate for a volume fraction between 0.4 to 0.6, with nanoparticle bricks with a higher absolute value. Platelets and cylindrical nanoparticles have lower heat transfer rates than those obtained for spherical nanoparticles for high volume fractions.

Figure 14 presents thermal irreversibility results, rep-

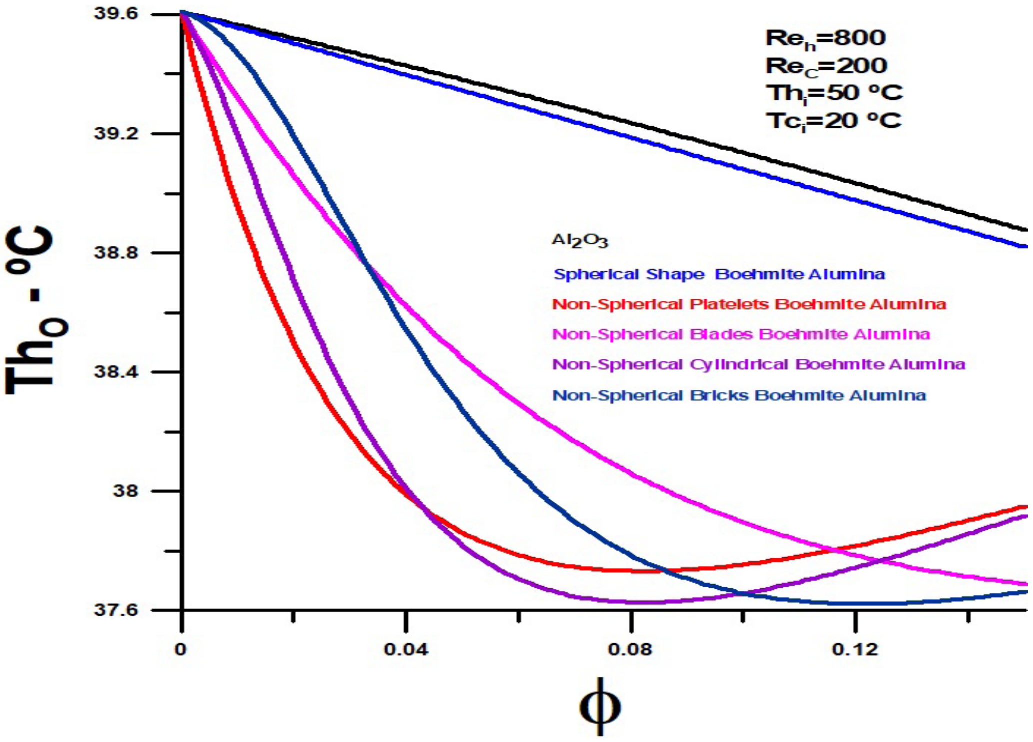

Figure 11. Fluid hot exit temperature versus volume fraction of nanoparticles number Re_h=800 and Re_c=200

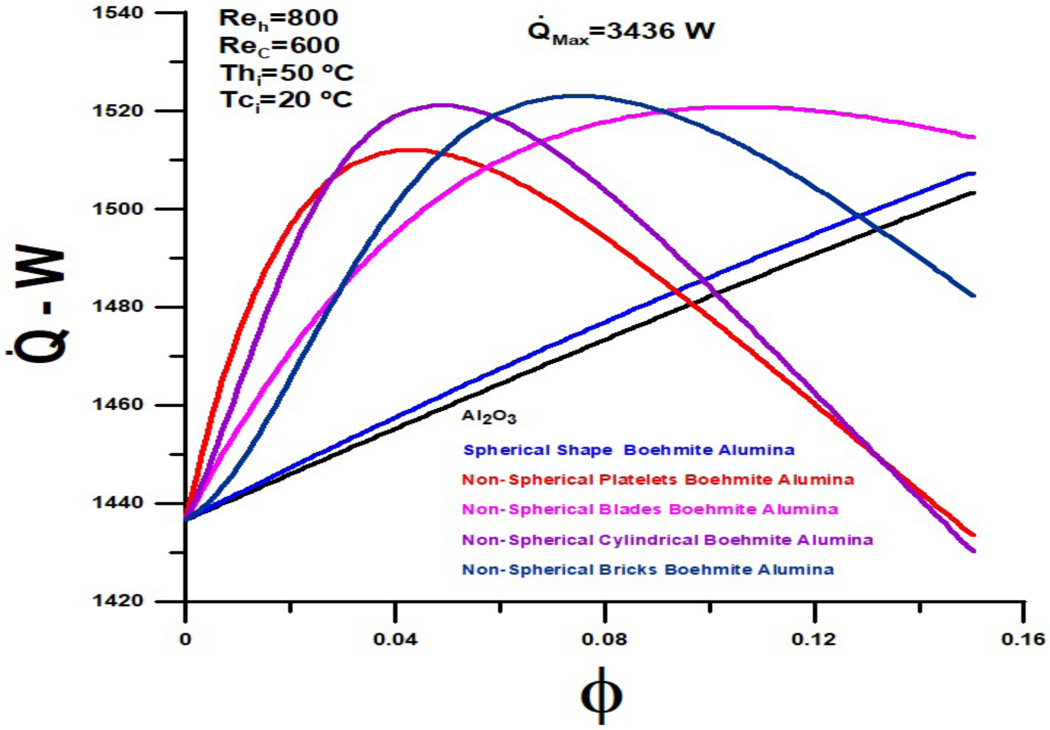

Figure 12. Heat transfer rate versus volume fraction of nanoparticles Re_h=800 and Re_c=600

resenting the generation of entropy, as a function of the volume fraction of the nanoparticles for Re_h=800 and Re_c=600. Values for thermal irreversibility are relatively low concerning total entropy, which considers the portion of entropy generation associated with the viscosity of the medium. Entropy generation grows with the volume fraction for all nanoparticles and is relatively high for non-spherical nanoparticles compared to entropy generation for spherical particles. The results, in this case, show numerical values more elevated than the situation already analyzed, Re_h=800 and Re_c=200, and reflect the higher heat transfer rate. The nanoparticle shapes affect the interaction between the fluid base and the nanoparticles. Greater irreversibility is achieved for non-spherical cylindrical and platelet nanoparticles for volume fraction small and medium values. The entropy generation rate did not reach the maximum for the non-spherical nanoparticles blade and brick, within the volume fraction range equal to 0.0 and 0.15. The maximum entropy generation for these non-spherical nanoparticles is reached at a volume fraction equal to 0.15.

Figure 15 presents results for thermal efficiency as a function of the volume fraction of the nanoparticles for Re_h=800 and Re_c=600. Efficiency is low where irreversibility is high, when heat transfer rate is high, or when there is high entropy generation.

Figure 16 shows the hot fluid outlet temperature as a function of the volume fraction of the nanoparticles and complements the information already obtained for Re_h=800 and Re_c=600. The hot fluid outlet temperatures are always lower than Re_h=800 and Re_c=200. The lowest outlet temperature occurs when irreversibility is high or greater heat exchange between the media, corresponding to non-spherical cylindrical and brick nanoparticles for volume fractions between 0.4 to 0.6. For blade and nanoparticles bricks, lower output temperature can be reached for a volume fraction between 0.6 to 0.15. The relevant fact is that the hot fluid exit temperature may be lower for spherical nanoparticles for high volume fractions.

Figures 17 and 18 present the hot fluid exit temperature values of the two different volume fractions. For a volume fraction equal to 0.05, the exit temperatures for non-spherical nanoparticles are, in all cases, lower than the exit temperatures for spherical nanoparticles. As already observed, for a fraction in a volume equal to 0.15, the only nanoparticle that present exit temperatures lower than those obtained for spherical nanoparticles are those that have the shape of the blade. The lowest exit temperatures for all nanoparticles are obtained for Re_h=200 and Re_c=200.

In summary, the results highlight platelets and cylindrical nanoparticles for Reynolds numbers Re_h=800 and Re_c=200 and demonstrate a higher heat transfer rate for low volume fractions. On the other hand, the brick and

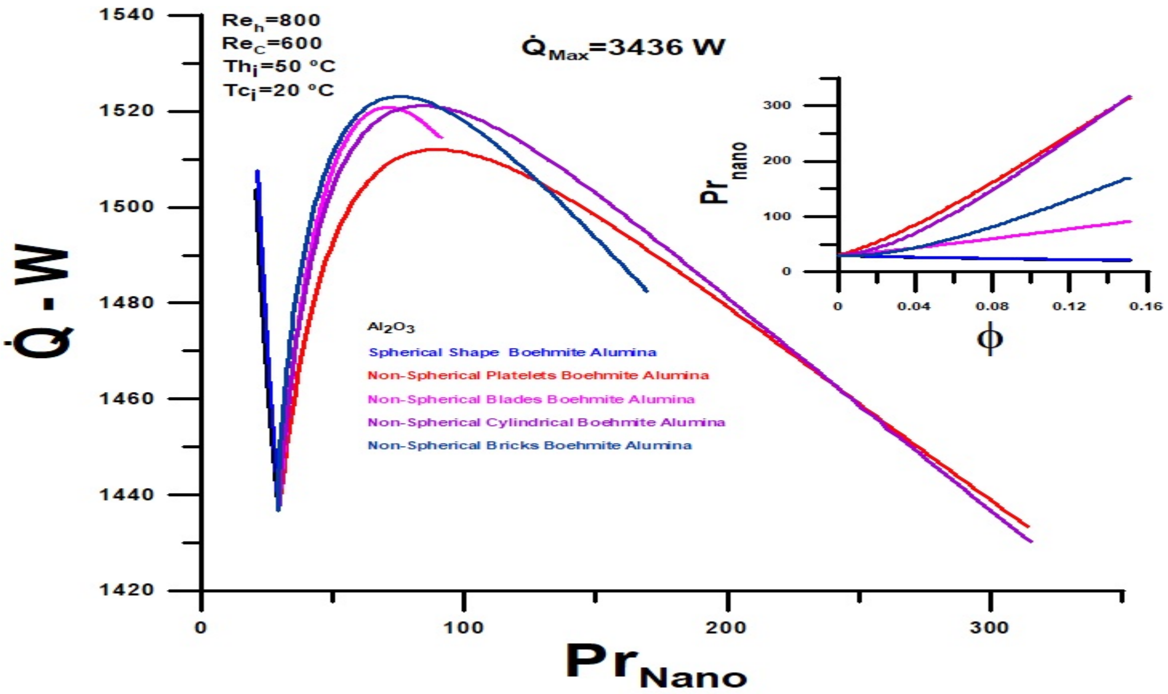

Figure 13. Heat transfer rate versus Prandtl number and Prandtl number versus volume fraction Re_h=800 and Re_c=600

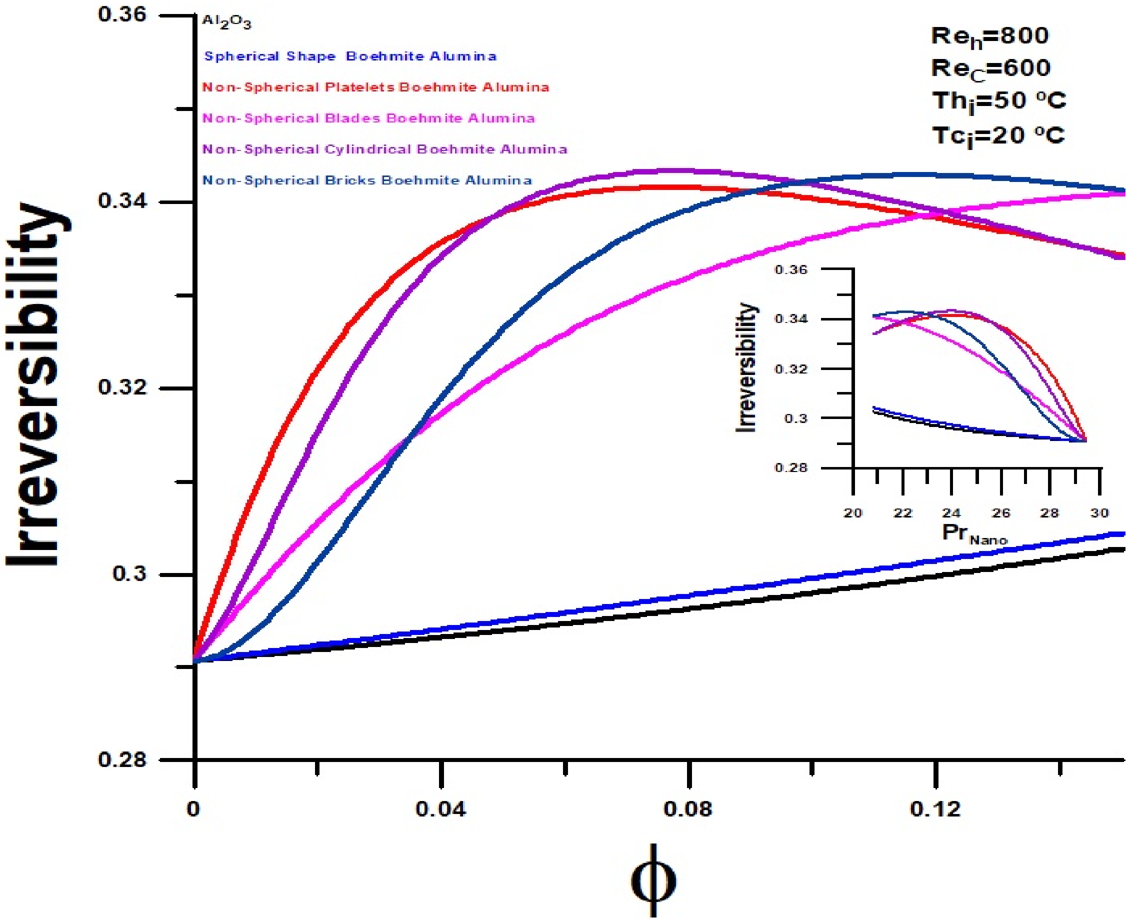

Figure 14. Irreversibility versus volume fraction of nanoparticles and Prandtl number Re_h=800 and Re_c=600

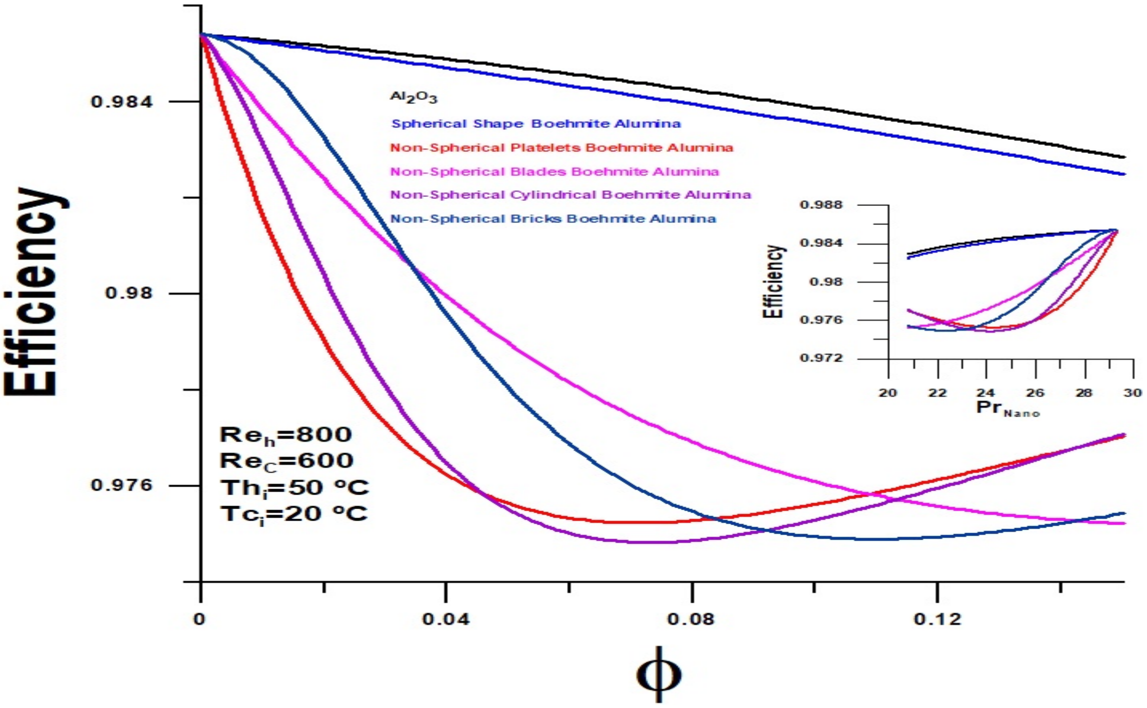

Figure 15. Efficiency versus volume fraction of nanoparticles and Prandtl number Re_h=800 and Re_c=600

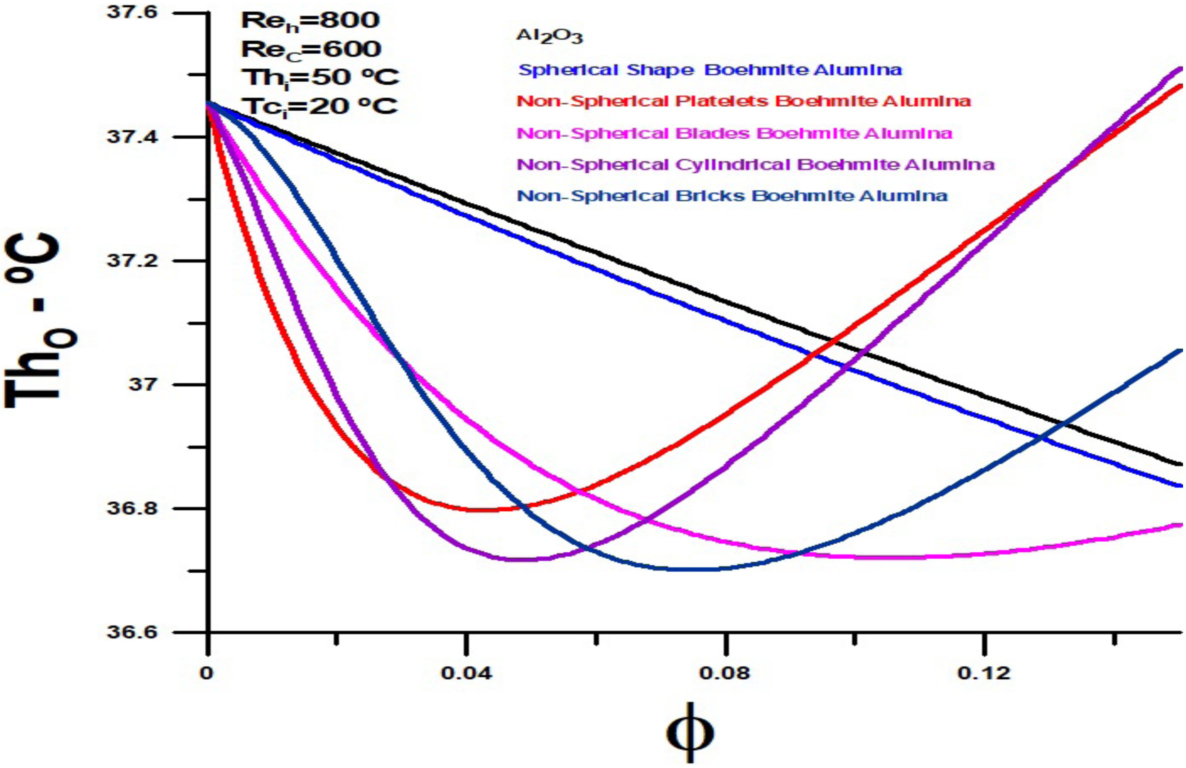

Figure 16. Fluid hot exit temperature versus volume fraction of nanoparticles Re_h=800 and Re_c=600

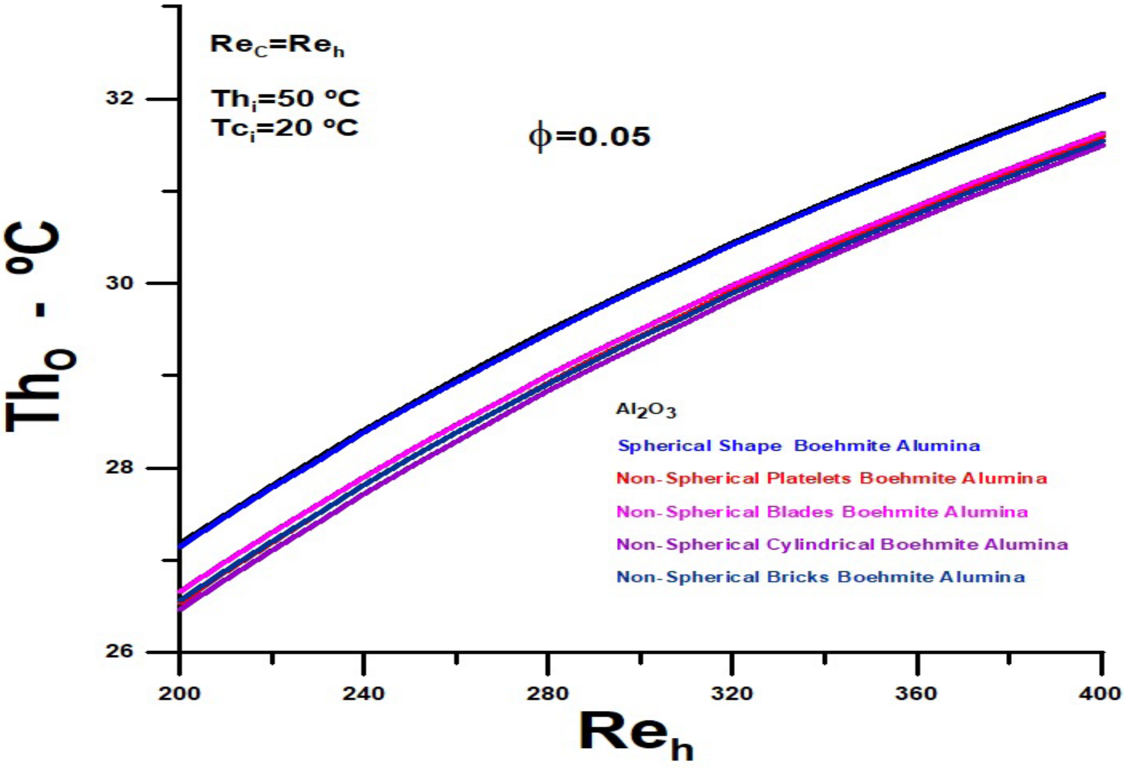

Figure 17. Fluid hot exit temperature versus Reynolds number for Φ=0.05

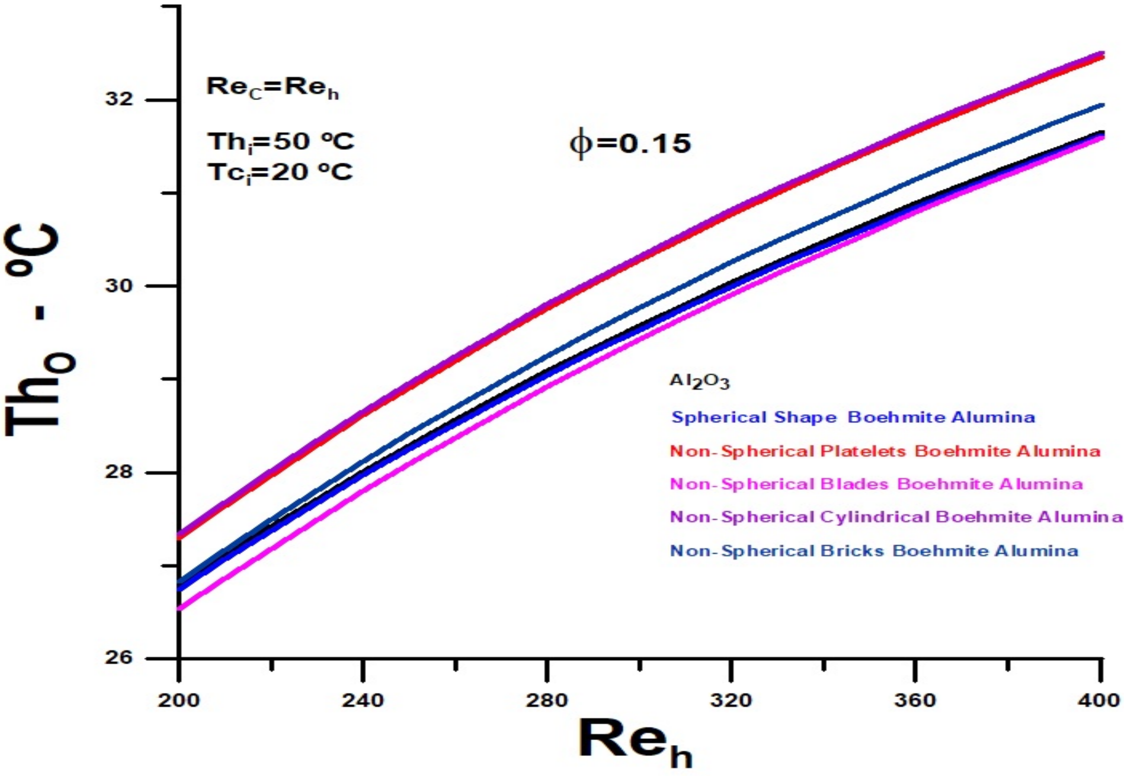

Figure 18. Fluid hot exit temperature versus Reynolds number for Φ=0.15

blade-shaped particles outperform the previous two for high volume fraction values. The non-spherical blade nanoparticle does not reach the maximum heat transfer value for the higher volume fraction under analysis equal to $\Phi = 0.15$.

For Reynolds numbers, Re_h=800 and Re_c=600 brick and blade nanoparticles have better thermal performance for volume fraction above 0.8, and non-spherical blade nanoparticle has a higher heat transfer rate than spherical nanoparticles across the entire volume fraction range analyzed. For a volume fraction above 0.10, platelets and cylindrical particles present the transfer rate below the value obtained for spherical nanoparticles. The lowest hot fluid exit temperature for brick and blade nanoparticles occurs for volume fractions between 0.6 to 0.15. Still, the hot fluid exit temperatures are always lower than Reh=800 and Rec=200 conditions.

4. Conclusions

The thermal performance of a printed circuit heat exchanger (PCHE) was determined using non-spherical nanoparticles compared to spherical nanoparticles. The analysis covered Reynolds values equal to 200 and 800 for the hot fluid and 200 and 600 for cold fluid, with volume fractions for the nanoparticles ranging from 0.05 to 0.15. The spherical particles are Al_2O_3 and Boehmite alumina, and the non-spherical particles of Boehmite alumina are platelets, blades, cylindrical, and bricks.

It was demonstrated that non-spherical particles have higher heat transfer rates than spherical particles. Applying the second law of thermodynamics methodology makes thermal performance analysis straightforward and elegant.

In specific terms, the work highlights:

- The nanoparticles' shapes affect the interaction between the fluid base and the nanoparticles, creating greater thermal irreversibility.

- Thermal entropy generation grows with the volume fraction for all nanoparticles and is relatively high for non-spherical nanoparticles than thermal entropy generation for spherical particles.

- The maximum theoretically possible heat transfer rate is associated with the hot fluid and serves as a reference for current heat transfer rates.

- Spherical nanoparticles present very close graphic results, as they have similar numerical thermodynamic properties.

- For volume fraction equal to 0.05, the hot fluid exit temperatures for non-spherical nanoparticles are in all cases lower than the hot exit temperatures for spherical nanoparticles.

- For a volume fraction equal to 0.15, the only nanoparticles that present lower hot fluid exit temperatures than those obtained for spherical nanoparticles are those that have the shape of a blade.

- For all nanoparticles under analysis, the lowest hot fluid exit temperatures are obtained for Re_h=200 and Re_c=200.

Conflict of Interest

The Author(s) declare(s) that there is no conflict of interest.

References

[1] Bejan, A., 1987. The thermodynamic design of heat and mass transfer processes and devices. Heat and Fluid Flow. 8(4), 258-276.

[2] Fakheri, A., 2007. Heat Exchanger Efficiency. Transactions of the ASME. 129, 1268-1276.
DOI: http://dx.doi.org/10.1016/j.applthermaleng.2017.05.076

[3] Tiwari, R., Maheshwari, G., 2017. Effectiveness and efficiency analysis of parallel flow and counter flow heat exchangers. IJAIEM. 6, 314-319.

[4] Nogueira, E., 2020. Thermal performance in heat exchangers by the irreversibility, effectiveness, and efficiency concepts using nanofluids. Journal of Engineering Sciences. 7, F1-F7.
DOI: https://doi.org/10.21272/jes.2020.7(2).f1.

[5] Nogueira, E., 2021. Efficiency and Effectiveness Thermal Analysis of the Shell and Helical Coil Tube Heat Exchanger Used in an Aqueous Solution of Ammonium Nitrate Solubility (ANSOL) with 20% H_2O and 80% AN. Journal of Materials Science and Chemical Engineering. 9, 24-45.
DOI: https://doi.org/10.4236/msce.2021.96003

[6] Chai, L., Tassou, S.A., 2020. A review of printed circuit heat exchangers for helium and supercritical CO_2 Brayton cycles. Thermal Science and Engineering Progress, 18(2020), 100543.
DOI: https://doi.org/10.1016/j.tsep.2020.100543

[7] Seo, J.W., Kim, Y.H., Kim, D., Choi, Y.D., Lee, K.J., 2015. Heat Transfer and Pressure Drop Characteristics in Straight Microchannel of Printed Circuit Heat Exchangers. Entropy. 17, 3438-3457.
DOI: https://doi.org/10.3390/e17053438

[8] Almurtaji, S., Ali, N., Teixeira, J.A., Addali, A., 2020. On the Role of Nanofluids in Thermal-Hydraulic Performance of Heat Exchangers—A Review. Nanomaterials. 10, 734.
DOI: https://doi.org/10.3390/nano10040734.

[9] Zahmakesh, I., Sheremet, M., Y., Heris, S.Z., Mohsen, S., Josua, P., Meyere, M.G., Wongwises, S., Jingj, D., Mahiankl, O., 2021. Effect of nanoparticle shape on the performance of thermal systems utilizing nanofluids: A critical review. Journal of Molecular Liquids. 321(1), 114430.
DOI: https://doi.org/10.1016/j.molliq.2020.114430

[10] Monfared, M., Shahsavar, A., Bahrebar, M.R., 2019. Second law analysis of turbulent convection flow of boehmite alumina nanofluid inside a double-pipe heat exchanger considering various shapes for nanoparticle. Journal of Thermal Analysis and Calorimetry. 135, 1521-1532.
DOI: https://doi.org/10.1007/s10973-018-7708-7

[11] Behrouz, R., Peyghambarzadeh, S.M., 2019. Measurement of Local Convective Heat Transfer Coefficient of Alumina-Water Nanofluids in a Double Tube Heat Exchanger. Journal of Chemical and Petroleum engineering. 53(1), 25-36.
DOI: https://doi.org/10.22059/jchpe.2019.265521.1247

[12] Elena, V., Timofeeva, J., Routbort, L., Dileep, S., 2009. Particle shape effects on thermophysical properties of alumina nanofluids. Journal of Applied Physics. 106, 014304.
DOI: https://doi.org/10.1063/1.3155999

[13] Zhou, X.F., 2006. Effective thermal conductivity in nanofluids of non-spherical particles with interfacial thermal resistance: Differential effective medium theory. Journal of Applied Physics. 100, 024913.
DOI: https://doi.org/10.1063/1.2216874

[14] Kays, W.M., London, A.L., 1984. Compact Heat Exchangers. MacGraw-Hill, New York.

Journal of Metallic Material Research
https://ojs.bilpublishing.com/index.php/jmmr

ARTICLE

Interpretation of Water Samples by Correspondence Analysis for Radioactive Elements in the Northern Coast of Oman Sea

Farshad Darabi-Golestan[1*] **Mohamad Reza Zare**[2]

1. Department of Mining and Metallurgical Engineering, Amirkabir University of Technology, Tehran, Iran
2. Department of Physics, Faculty of Sciences, University of Isfahan, Isfahan, 81746-73441, Iran

ARTICLE INFO

Article history
Received: 29 March 2022
Accepted: 24 April 2022
Published Online: 5 May 2022

Keywords:
Hormoz canyon
R-mood analysis
Correspondence analysis
Radioactive elements
Marine spot samples

ABSTRACT

Oman Sea is connecting belt between the Indian Ocean and Persian Gulf. Because it strategic and environmental aim, presence of natural radionuclide ^{226}Ra, ^{232}Th, ^{40}K and ^{137}Cs as man-made element is considered. Water samples were taken from 36 marine spots at the coastal strip from Hormoz canyon to Goatr seaport in the northern coast of Oman Sea. Correspondence analysis is used to identify variation and relationship between samples (Q-mood analysis) and variable (R-mood analysis) based on approximate χ^2 distances. Radioactive elements (^{226}Ra, ^{232}Th and ^{40}K), physical (temperature, pH, turbidity, conductivity, special density) and chemical (salinity, oxygen and chlorophyll) parameters of water for 36 samples handled by correspondence analysis, there are two outstanding result, 1) Radioactive elements show high correlation in factors by greater eigenvalue, and 2) some of the samples such as W13, W24 and rather W02, W05 and W12 show highest activity from Radioactive elements and also temperature and conductivity show nearest relation with them in many factors.

1. Introduction

The radionuclides are the source of natural radioactivity in earth [1,2]. Some effective dose of natural radioactivity received by human acts in the world. Large amounts of radionuclides have been released into the environment after the Fukushima and Chernobyl nuclear accidents [3]. The current research tries to create a reference value to future investigation. Therefore, the data can be basic values in the region, while the results always are comparable data in each. It was necessary to mention that this the same type of this research was published for many countries, such as Ireland, Egypt [4,5], India [6], China [7], America [8], Turkey [9] and Mexico [10]. According to the International Atomic Energy Agency (2003) [11], the standard systematic sampling was taken at the northern coastline of Oman Sea.

Water quality assessment studies, especially in coastal seas from natural radionuclides have been frequently conducted in many countries at the last years [12,13]. The

---

*Corresponding Author:
Farshad Darabi-Golestan,
Department of Mining and Metallurgical Engineering, Amirkabir University of Technology, Tehran, Iran;
Email: pooyan@aut.ac.ir

DOI: https://doi.org/10.30564/jmmr.v5i1.4571

variables and samples analysis were done by Correspondence Analysis (CA) according to covariance and distance parameters from R-mode and Q-mode analysis respectively [14-16]. Accordingly, indicator samples were adjusted in the spatial neighborhood of related variables [17]. Monitoring of the radioactivity for all radionuclides is the main environmental aim at each country. Besides these data could be considered as reference data to check the radioactivity changes during too many years. During this study, the interaction effect of conductivity, temperature, special density, salinity, chlorophyll, oxygen, turbidity and pH parameters against ^{226}Ra, ^{232}Th and ^{40}K radionuclides has been considered using multivariate analysis. Some of these parameters show best similarity to detect radionuclide concentrations.

2. Materials and Methods

The total number of 36 marine spot was designed in the northern coast of Oman Sea. The first related sample was taken from the Hormoz canyon and it continued by coastal strip to Goatr seaport. The sampling project was done in May 2011 and covered an area between 56° 30′ to 61° 30′ in longitude and 25° to 26° in latitude. Figure 1 shows the location of sampling spots, afterward the sample code and location of each sample represented in Table 1. A hand-held EXPLORANIUM spectrometer was applied to monitoring and detect the environmental changes [18,19]. By using the CTD system could record conductivity (MS/cm), temperature (°C), special density (gr/cm^3), salinity (PSU), chlorophyll (mgr/m^3), oxygen (PPM), turbidity (NTU) and pH of water. A suitable pump was used to suction about 100 liters of surface water from the Oman gulf. A container applied to minimize the absorption of activity. Accordingly, the pH of water solution decreases to 1.5 and High-Purity Germanium (HPGe) are used to detect of high-precision digital electronics of all parameters [6-20]. The portable HPGe detector positioned vertically inverse at center of the water sample [21,22]. All samples were taken from the nearest coastal strip and each spot designed which could probe possible polluting sources. All the statistic and multivariate analysis are done using Minitab 19.2020.1 (64-bit) and SPSS Statistics 17.

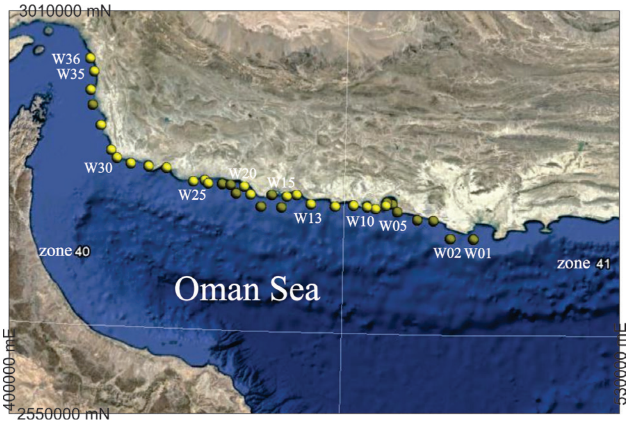

Figure 1. Locations map of the sampling spots consist of water samples

Table 1. The location of water samples in Oman Sea

Sample code	location	Sample code	location
W01	Chabahar Seaport (Pasabandar)	W19	Pi Bashk (Karti)
W02	Chabahar Seaport (Baris Bala)	W20	Pi Bashk (Lirdaf)
W03	Chabahar Seaport (Baris Bala)	W21	Pi Bashk (Sadich)
W04	Chabahar Seaport	W22	Pi Bashk (Sadich)
W05	Chabahar Seaport	W23	Pi Bashk (Kentaki)
W06	Chabahar Seaport (Konarak)	W24	Pi Bashk (Kentaki)
W07	Chabahar Seaport (Konarak)	W25	Pi Bashk (Kentaki)
W08	Chabahar Seaport (Konarak)	W26	Jask Seaport
W09	Chabahar Seaport (Konarak)	W27	Jask Seaport
W10	Chabahar Seaport (Konarak)	W28	Jask Seaport
W11	Chabahar Seaport (Gordim)	W29	Jask Seaport
W12	Pi Bashk (Tong Seaport)	W30	Jask Seaport
W13	Pi Bashk (Hoomadan)	W31	Jask Seaport
W14	Pi Bashk (Derak)	W32	Taherooi (Serich)
W15	Pi Bashk (Derak)	W33	Taherooi (Mashi)
W16	Pi Bashk (Derak)	W34	Taherooi (Mashi)
W17	Pi Bashk (Karti)	W35	Taherooi (Sirik Seaport)
W18	Pi Bashk (Karti)	W36	Gheshm

3. Results

3.1 Statistical Analysis

The minimum and maximum, mean and median, standard deviation, variance, values of ^{226}Ra, ^{232}Th and ^{40}K are showed in Table 2. The boxplot that displays the distribution of median confidence interval box, outlier symbols, median symbol and the minimum and maximum, mean for Ra, Th, and K (Figure 2).

3.2 Correspondence and K-means Analysis

Correspondence Analysis (CA) method is a useful method in order to geochemical classification of variables [23,24]. By application of this method could reduce high-dimensional data into subset of data which have low-dimension. These data could easily interpret and show effective and simple dimension. The subspaces reveal the main variances between variables [25-28]. R-mode and Q-mode are the two main branches of CA method [28,29]. The Q-mode (represented as sample-to-sample analysis) and R-mode (represented as element-to-element) are the two main results of the CA analysis. The results of R-mode and Q-mode matrix are combined as F-matrix while the distances are χ^2 distances between the respective modes [30,25]. Therefore, the CA could easily indicate the similarity or association between variables (R-mode, which represented by loadings or blue vectors in Figure 3) derived from data samples (Q-mode, which represented by scores or red symbols in Figure 3). The first (82% of Inertia) and second (9.6% of Inertia) CA factors with the highest eigenvalue are the stronger factors. The cumulative proportion of inertia for the first and second factor consists of 91.5% of total variation in the whole samples (Table 3). The symmetric with combination of the first and second factor is displayed in Figure 2. Both row and column principal coordinate overlaid in new dimensions. This method could ease difficulty between variables while there are not of primary interest in data (for columns and rows). Therefore, columns (variables) and rows (samples) plotted in new dimension.

Table 2. Descriptive statistics of water samples for ^{226}Ra, ^{232}Th and ^{40}K activity concentration.

	Variable	Minimum	Maximum	Mean	Median	St.Dev.	Variance
water sample (Bq/Lit)	^{226}Ra	2.19	2.82	2.4917	2.555	0.1794	0.0322
	^{232}Th	1.66	2.17	1.9031	1.885	0.1514	0.0229
	^{40}K	132.6	148.87	141.48	144.42	5.87	34.51

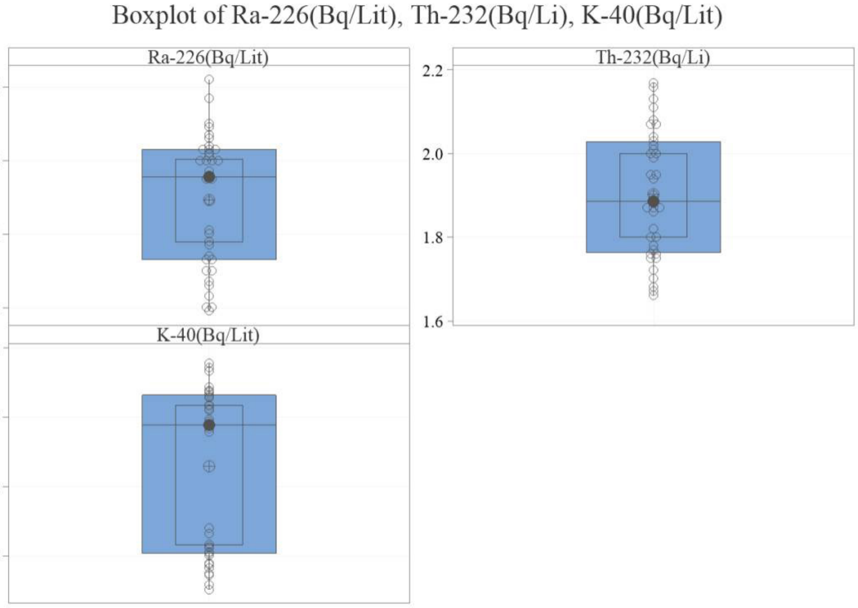

Figure 2. The boxplot of Ra, Th and K for water samples

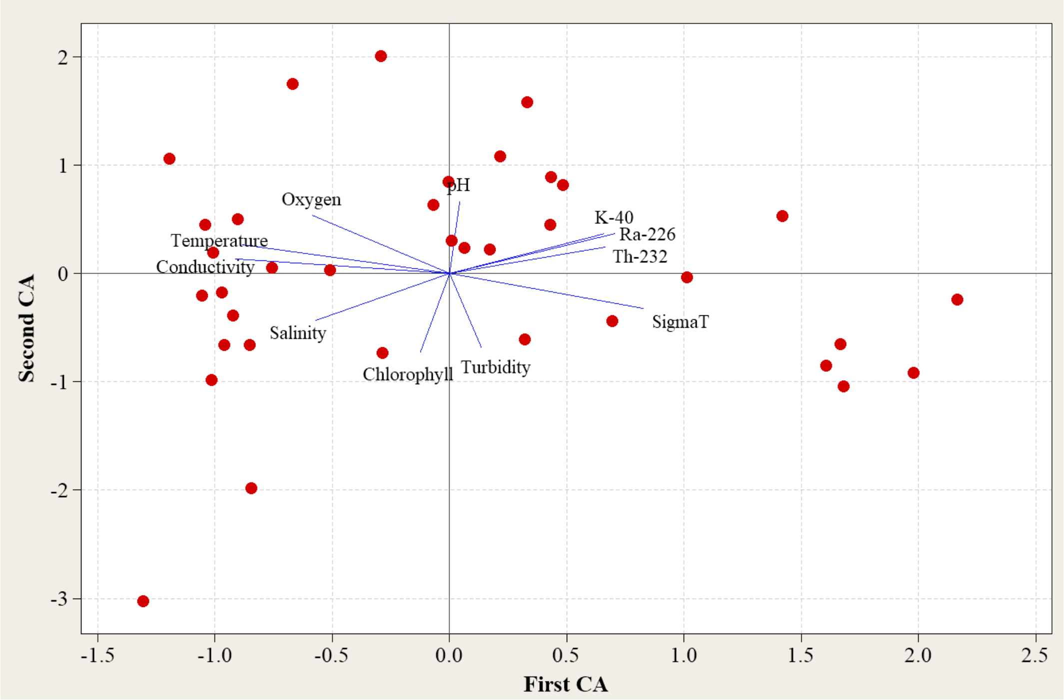

Figure 3. The 2-D symmetric plot from multivariate CA analysis for the first and second dimensions in the water samples.

The parameters and radionuclides are plotted within new dimension according to Euclidian distances between observations by covariance-based and distance-based analysis. *Symbols are the special dispersion pattern of sample in the new dimension that represent amount of concentration in samples.

Table 3. The Contingency table from CA analysis

Axis	Inertia	Proportion ratio	Cumulative
1	0.0094	0.8190	0.8190
2	0.0011	0.0961	0.9151
3	0.0007	0.0629	0.9780
4	0.0001	0.0125	0.9906

4. Discussion

A set of samples in a K-means cluster are more similar to each other according to some similarity or dissimilarity measures. Therefore, it was used and revealed that samples show different properties due to their parameters. All samples were categorized in 4 groups (Figure 4), while the first group (which have 13 observations) shows higher value for Ph, K, Ra, Th. The second and the third group have 7 and 8 samples, respectively. They are more important for temperature, conductivity, salinity. Parameters. The fourth group by 8 samples show higher turbidity and sigma-T. The first dimension of CA indicates maximum variance between ^{226}Ra, ^{232}Th and ^{40}K parameters and temperature, sigma-T, oxygen, conductivity. On the other hand, the second dimension of CA analysis indicates different Eigenvector for pH, turbidity, chlorophyll, and salinity parameters.

The sample numbers of W13, W18 and W24 are strongly, in which W12, W05 and W02 are moderately concentrated from ^{226}Ra, ^{232}Th and ^{40}K radionuclides (Figure 4). According to the Figure 2 it would have revealed that sample W13 and W18 (Eigenvalues distinguished by black circles, Figure 4) have been concentrated from ^{226}Ra, ^{232}Th and ^{40}K radionuclides (shown by blue eigenvectors, Figure 3), whereas, W26 and W03 show at least values. On the other hand, W26 and W35 sample numbers considered as the highest values of salinity and chlorophyll. All the water variation from radionuclides indicated by the 2D graphical representation of eigenvalues and eigenvectors (Figure 3), simultaneously in the correspondence (CA) and factor analysis combination. The sample numbers of W18, W34, W21, W08, W04, W13 and W24 can straighten this idea. Also, the second dimension of variation in CA indicates that turbidity, chlorophyll, and salinity have the minimum similarities with ^{226}Ra, ^{232}Th and ^{40}K radionuclides and it is indicated according to W26 and W35 samples. During this paper concluded that Sigma-T and pH considered as best indicator for radionuclides concentration. Higher concentrated values for salinity and conductivity may be originated from at least values for ^{226}Ra, ^{232}Th and ^{40}K radionuclides.

Activity concentrations of radionuclides of ^{40}K, ^{226}Ra and ^{232}Th were measured (Table 2) and results compared with international standard values and legal regulations (Table 4). Maximum activity concentration of ^{226}Ra and ^{40}K was measured respectively 2.82 Bq/Lit and 148.87 Bq/Lit in sample number 13 at Pi Bashk (Hoomadan). Accordingly, the maximum value of ^{232}Th was 2.17 Bq/Lit in sample number W34 at Taherooi (Mashi). The natural activity concentrations of radionuclides of ^{40}K, ^{226}Ra, and ^{232}Th have been estimated below the significant values in the world.

Table 4. The compression of concentrations of K, Ra and Th northern coast of Oman sea with international standard values and legal regulations

Country	^{40}K	^{232}Th	^{226}Ra	References
Nigeria	7.51±0.56	1.78±0.14	2.99±0.57	[31]
Earth’s crust average	400	30	-	[32]
Albania (minimum-maximum)	266-675	13-40	13-23	[33]
India, East coast of Tamilnadu (CSS)	360.23	14.29	-	[34]
Saudi coastline, Gulf of Aqaba (CSS)	641.1	22.5	-	[35]
Greateraccra, Ghana (CSS)	29.78	108.6	-	[36]
Egypt red sea (Marine sediment)	330.70 ± 107	16.19 ± 8.68	-	[37]
Iran (Anzali wetland) (minimum-maximum)	371.8-652.28	17.57-45.84	13.83-38.37	[38]
Iran (northern coast of Oman Sea, CSS)	141.48	1.9031	2.4917	Present study

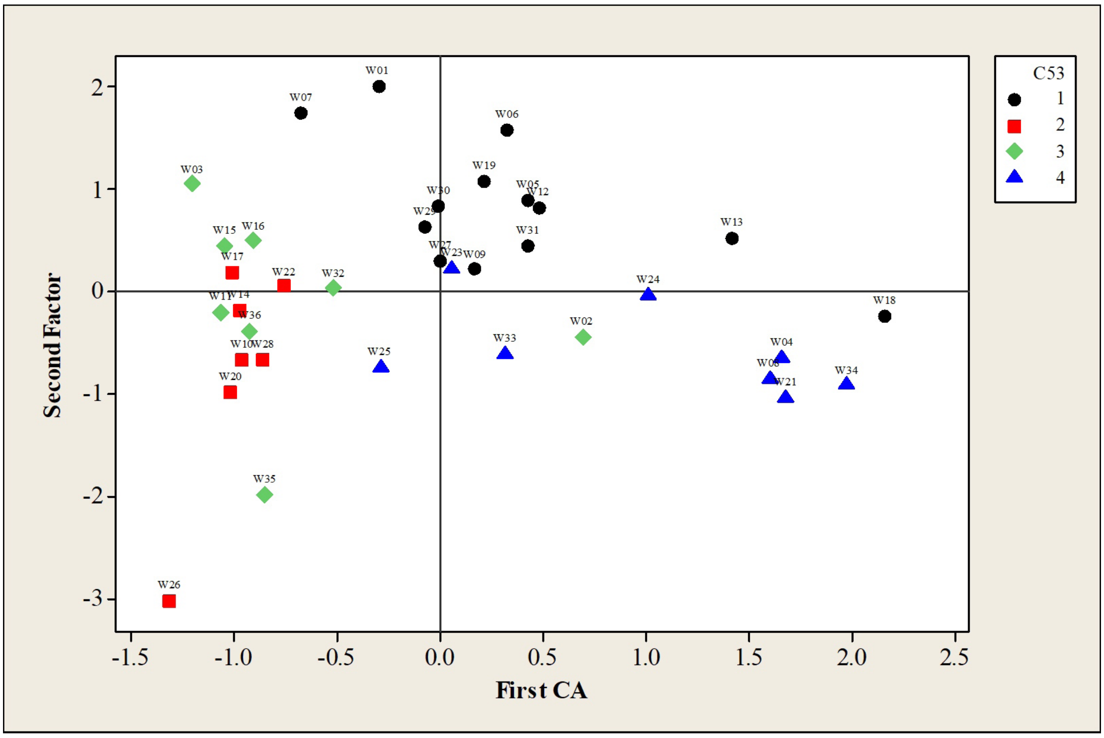

Figure 4. The graphical combination plot of CA and K-means clustering.

5. Conclusions

Correspondence analysis is applied to recognize water sample and analyzed variable (three radioactive element and eight physical and chemical properties of sample). In these surveys, variables of Ra, Th and K have different specification from conductivity, temperature, special density, salinity, chlorophyll, oxygen, turbidity and pH of water. Accordingly, these radionuclides have same behavior (with high eigenvalue) and correlated in stronger factors. Therefore, samples such as W13, W24, W18 (strongly) and W12, W05 and W02 (moderately) are concentrated from Th, Ra and K. By application of CA and factor multivariate analysis, the first dimension shows the conductivity, temperature, O_2 and salinity parameters have distinctly different from ^{226}Ra, ^{232}Th and ^{40}K according to covariance-based (R-mode) analysis. On the other hand, the second dimension indicates temperature, O_2, and conductivity and maybe pH have a high correlation with radionuclides. Finally, after analysis, the values of the ^{226}Ra, ^{235}U, ^{40}K, ^{232}Th, and ^{137}Cs concentrations in water samples were lower than that value of the world. Therefore, the data can be basic values in the region and accepted as a reference and comparable data in each time. During this paper concluded that Sigma-T and pH considered as best indicator for radionuclides concentration. Higher concentrated values for salinity and conductivity may be originated from at least values for ^{226}Ra, ^{232}Th and ^{40}K radionuclides. Regarding these parameters, all the data are below the significant values in the world but it suggested that Pi Bashk (Hoomadan) and Taherooi (Mashi) stations need to be studied in the future.

Conflict of Interest

There is no conflict of interest.

References

[1] Abdi, M., Faghihian, H., Mostajaboddavati, M., et al., 2006. Distribution of natural radionuclides and hot points in coasts of Hormozgan, Persian Gulf, Iran. Journal of Radioanalytical and Nuclear Chemistry. 270(2), 319-324.

[2] Alatise, O., Babalola, I., Olowofela, J., 2008. Distribution of some natural gamma-emitting radionuclides in the soils of the coastal areas of Nigeria. Journal of Environmental Radioactivity. 99(11), 1746-1749.

[3] Matisoff, G., Ketterer, M.E., Rosén, K., et al., 2011. Downward migration of Chernobyl-derived radionuclides in soils in Poland and Sweden. Applied Geochemistry. 26(1), 105-115.

[4] Harb, S., 2008. Natural radioactivity and external gamma radiation exposure at the coastal Red Sea in Egypt. Radiation Protection Dosimetry. 130(3), 376-384.

[5] Uosif, M., El-Taher, A., Abbady, A.G., 2008. Radiological significance of beach sand used for climatotherapy from Safaga, Egypt. Radiation Protection Dosimetry. 131(3), 331-339.

[6] Gouda, M., Hamzawy, A., Badawi, M., et al., 2016. Mathematical method to calculate full-energy peak efficiency of detectors based on transfer technique. Indian Journal of Physics. 90(2), 201-210.

[7] Xu, L., Liu, X., Sun, L., et al., 2010. Distribution of radionuclides in the guano sediments of Xisha Islands, South China Sea and its implication. Journal of Environmental Radioactivity. 101(5), 362-368.

[8] Myrick, T., Berven, B., Haywood, F., 1983. Determination of Concentrations of Selected Radionuclides in Surface Soil in the US. Health Physics. 45(3), 631-642.

[9] Kurnaz, A., Küçükömeroğlu, B., Keser, R., et al., 2007. Determination of radioactivity levels and hazards of soil and sediment samples in Fırtına Valley (Rize, Turkey). Applied Radiation and Isotopes. 65(11), 1281-1289.

[10] Mireles, F., Davila, J., Quirino, L., et al., 2003. Natural soil gamma radioactivity levels and resultant population dose in the cities of Zacatecas and Guadalupe, Zacatecas, Mexico. Health Physics. 84(3), 368-372.

[11] International Atomic Energy Agency, 2003. Collection and Preparation of Bottom Sediment Samples for Analysis of Radionuclides and Trace Elements. IAEA-TECDOC 1360, IAEA, Vienna (technical report).

[12] Yasmin, S., Barua, B.S., Kamal, M., et al., 2014. An Analysis for Distribution of Natural Radionuclides in Soil, Sand and Sediment of Potenga Sea Beach Area of Chittagong, Bangladesh. Journal of Environmental Protection. 5(17), 1553.

[13] Zare, M.R., Kamali, M., Kapourchali, M.F., et al., 2016. Investigation of ^{235}U, ^{226}Ra, ^{232}Th, ^{40}K, ^{137}Cs, and heavy metal concentrations in Anzali international wetland using high-resolution gamma-ray spectrometry and atomic absorption spectroscopy. Environmental Science and Pollution Research. 23(4), 3285-3299.

[14] Aggrawal, D., Bansal, G., Anand, A., et al., 2016. Types of Customers Surrounding a Brand: A Classification Based on Correspondence Analysis. Communications in Dependability and Quality Management. 19(1), 5-17.

[15] Darabi-Golestan, F., Hezarkhani, A., 2018. Evaluation of elemental mineralization rank using fractal and multivariate techniques and improving the per-

formance by log-ratio transformation. Journal of Geochemical Exploration. 189, 11-24.

[16] Wang, C.H., 2016. A novel approach to conduct the importance-satisfaction analysis for acquiring typical user groups in business-intelligence systems. Computers in Human Behavior. 54, 673-681.

[17] Kumru, M., Bakac, M., 2003. R-mode factor analysis applied to the distribution of elements in soils from the Aydın basin, Turkey. Journal of Geochemical Exploration. 77(2), 81-91.

[18] Collins, S.V., Boyce, J.I., 2004. Discriminant Function Analysis of Spectral Gamma Data as a Tool for Regional Stratigraphic Correlation of Pleistocene Deposits. AGU Spring Meeting Abstracts. pp. H41D-06.

[19] Swoboda, M., Arlt, R., Gostilo, V., et al., 2005. Spectral gamma detectors for hand-held radioisotope identification devices (RIDs) for nuclear security applications. IEEE transactions on nuclear science. 52(6), 3111-3118.

[20] Wershofen, H., Arnold, D., 2005. Radionuclides in Ground-level Air in Braunschweig: Report of the PTB Trace Survey Station from 1998 to 2003, Physikalisch-Technische Bundesanstalt.

[21] Darabi-Golestan, F., Hezarkhani, A., Zare, M., 2017. Assessment of ^{226}Ra, ^{238}U, ^{232}Th, ^{137}Cs and ^{40}K activities from the northern coastline of Oman Sea (water and sediments). Marine Pollution Bulletin. 118(1), 197-205.

[22] Darabi-Golestan, F., Hezarkhani, A., 2020. Discrimination geochemical interaction effects on mineralization at the polymetallic Glojeh deposit, NW Iran by interative backward quadratic modeling. Acta Geochimica. 39(2), 236-254.

[23] Belkhiri, L., Narany, T.S., 2015. Using multivariate statistical analysis, geostatistical techniques and structural equation modeling to identify spatial variability of groundwater quality. Water Resources Management. 29(6), 2073-2089.

[24] Deutsch, J.L., Palmer, K., Deutsch, C.V., et al., 2016. Spatial Modeling of Geometallurgical Properties: Techniques and a Case Study. Natural Resources Research. 25(2), 161-181.

[25] Akbarpour, A., Gholami, N., Azizi, H., et al., 2013. Cluster and R-mode factor analyses on soil geochemical data of Masjed-Daghi exploration area, northwestern Iran. Arabian Journal of Geosciences. 6(9), 3397-3408.

[26] Bu, C.F., Zhang, P., Wang, C., et al., 2016. Spatial distribution of biological soil crusts on the slope of the Chinese Loess Plateau based on canonical correspondence analysis. Catena: An Interdisciplinary Journal of Soil. 137, 373-381.

[27] Carranza, E.J.M., 2009. Controls on mineral deposit occurrence inferred from analysis of their spatial pattern and spatial association with geological features. Ore Geology Reviews. 35(3), 383-400.

[28] Darabi-Golestan, F., Hezarkhani, A., 2019. Multivariate analysis of log-ratio transformed data and its priority in mining science: Porphyry and polymetallic vein deposits case studies. Bulletin of the Mineral Research and Exploration. 159(159), 185-200.

[29] Ji, H., Zeng, D., Shi, Y., et al., 2007. Semi-hierarchical correspondence cluster analysis and regional geochemical pattern recognition. Journal of Geochemical Exploration. 93(2), 109-119.

[30] Abdi, H., Valentin, D., 2007. Multiple correspondence analysis. Encyclopedia of measurement and statistics. pp. 651-657.

[31] Anekwe, U.L., Ibe, S.O., 2021. Natural Radioactivity in Some Borehole Water in Ogbia Local Government Area, Bayelsa State, Nigeria.

[32] UN Scientific Committee on the Effects of Atomic Radiation, 2000. Sources and effects of ionizing radiation. New York: United Nations Publications.

[33] Tsabaris, C., Eleftheriou, G., Kapsimalis, V., et al., 2007. Radioactivity levels of recent sediments in the Butrint Lagoon and the adjacent coast of Albania. Applied Radiation and Isotopes. 65(4), 445-453.

[34] Ravisankar, R., Chandramohan, J., Chandrasekaran, A., et al., 2015. Assessments of radioactivity concentration of natural radionuclides and radiological hazard indices in sediment samples from the East coast of Tamilnadu, India with statistical approach. Marine Pollution Bulletin. 97(1), 419-430.

[35] Al-Trabulsy, H., Khater, A., Habbani, F., 2011. Radioactivity levels and radiological hazard indices at the Saudi coastline of the Gulf of Aqaba. Radiation Physics and Chemistry. 80(3), 343-348.

[36] Amekudzie, A., Emi-Reynolds, G., Faanu, A., et al., 2011. Natural radioactivity concentrations and dose assessment in shore sediments along the coast of Greater Accra, Ghana. World Applied Sciences Journal. 13(11), 2338-2343.

[37] Dar, M.A., El Saman, M.I., 2012. The radiation hazards of some radio-elements in petroleum and phosphate regions along the Red Sea, Egypt. Proceeding of The Third International on Radiation Sciences and Applications. 5(2), 920.

[38] Darabi-Golestan, F., Hezarkhani, A., Zare, M.R., 2019. Geospatial analysis and assessment of ^{226}Ra, ^{235}U, ^{232}Th, ^{137}Cs, and ^{40}K at Anzali wetland, north of Iran. Environmental Monitoring and Assessment. 191(6), 1-15.

BILINGUAL PUBLISHING CO.
Pioneer of Global Academics Since 1984

Journal of Metallic Material Research
https://ojs.bilpublishing.com/index.php/jmmr

ARTICLE

Determination of Hydrodynamic Parameters of Chitosan Stabilized Bimetallic Nanoparticles

Vokhidova N.R.[*] **Rashidova S.Sh.**

Institute of Chemistry and Physics of Polymers of Scientific Academy of Uzbekistan, Uzbekistan

ARTICLE INFO

Article history
Received: 28 March 2022
Accepted: 27 April 2022
Published Online: 29 April 2022

Keywords:
Chitosan *Bombyx mori*
Bimetallic nanoparticles
Index polydispersity
Diffusion coefficient

ABSTRACT

The hydrodynamic characteristics of bimetallic Ag/Cu and Co/Ag nanoparticles stabilized by chitosan were determined. The polydispersity index and the diameter of nanoparticles were observed to decrease in contrast to the original polymer during the creation of chitosan stabilized bimetallic nanoparticles, decreasing from 0.342 to 0.12±0.04 and 2.5 micron to 180 nm, respectively. However, the diffusion coefficient of chitosan was increased from 0.2 cm^2/s to 2.71 cm^2/s during the production of stable bimetallic nanoparticles. The lack of absorption bands at 500 nm and 700 nm-900 nm in the UV spectra of the samples suggests that in the presence of a reducing agent, copper (II) and cobalt (II) ions undergo full reduction. The relationship between the synthesis conditions and the kind of structure of bimetallic nanoparticles "core-shell" has been discovered. Silver atoms have been shown to be both a core and a shell, depending on the synthesis conditions and chemical nature of metal ions.

1. Introduction

Different metal atoms create bimetallic nanoparticles (BNPs) and/or heteronuclear metal complexes, which have better mechanical and catalytic performance than monometallic complexes due to their synergistic functionalities and their intriguing biological and operational features, bimetallic complexes, particularly BNPs, have lately gained a lot of interest [1-4]. In this sense, there has lately been a trend toward using bimetallic compounds in relation to their potential in medicine. In a bimetallic complex, each metal center contributes according to its chemical characteristics, resulting in a boost in the complex's antibacterial capabilities above its monometallic counterpart.

BNPs are complexes with qualities that are significantly superior to those of their constituents. The usage of noble metals and the first-row transition value, in particular, are gaining popularity for applications in catalysis, electrocatalysis, and magnetism. Because of their capacity to form intermetallic phases, random alloys, and core-shell species, such objects have a diverse structural chemistry. Under impact on the surface, however, the nanostructure can be altered due to the observation, segregation, or

---

*Corresponding Author:
Vokhidova N.R.,
Institute of Chemistry and Physics of Polymers of Scientific Academy of Uzbekistan, Uzbekistan;
Email: noira_vokhidova@yahoo.de

DOI: https://doi.org/10.30564/jmmr.v5i1.4566

isolation of many atoms, resulting in the formation of a structure with higher catalytic activity [5].

In comparison to metallic nanoparticles, the production, physicochemical characteristics, and uses of bimetallic nanoparticles based on noble and transition metals are now intensively addressed. As a result, BNPs outperform their metallic counterparts in terms of biological, chemical, and mechanical qualities. BNPs Au/Ag, Ni/Pd, Au/Pd, and Au/Pt in the size range of 1 nm-100 nm have been reported to find specialized uses in diagnostics (bioimaging), biosensors, treatment, and drug delivery systems as a result of these features [6-8]. The size and distribution of bimetallic nanoparticles, shape, the ratio of two metals, and the internal distribution of metals in individual nanoparticles, for example, the presence of homogeneous alloys, core-shell systems, and other types of bimetallic nanoparticles are all important parameters for characterization [6].

One of the most essential features of their utilization is the fabrication of nanostructure catalysts based on bimetallic nanoparticles. It's probable that the synergistic impact of BNPs, in which they're interlinked at the atomic level and create diverse structures like alloys, core-shells, heterodimers, and so on, is linked to the effectiveness of bimetallic catalysts. The kinetics of catalysis can be affected by variations in the electronic state of metal centers in such materials [7].

As a result, BNP structure may be split into two categories: mixed structures and segregated structures. BNPs may be classified into four categories based on their atomic ordering: alloys, intermetallic compounds, subclusters, and shell-cores (core-shells, materials with several cores covered with one shell). BNP structures are created when two distinct elements are combined with a random mechanism of dispersion or nuclear envelope creation, such as mixed and random alloys, subclusters with two, three, or a small number of A-B bonding interfaces, and core-shell type at others [8-10].

The researchers created spherical bimetallic Ag/Fe nanoparticles of the "core-shell" type with a diameter of 136.3 nm that were bactericidal against multiresistant bacteria. It was discovered that BNPs Ag/Fe had better bioactivity against yeast and gram-positive and gram-negative bacteria than silver and iron mono-NPs. The link between "structure-bactericidal activity" and the prevention and treatment of infections caused by clinically important drug-resistant strains has been demonstrated [11].

Metal-containing nanomaterials, such as mono- and bimetallic nanoparticles, oxide nanoparticles with bioactive qualities that range in composition and properties, are currently in high demand in the nanoindustry [12-14]. BNPs appear to be crucial and promising nanomaterials in catalysis, medicine, agriculture, photocatalysis, and other fields. They differ from one other in composition and structure, as well as core-shell type, composition and structural dependent properties. Nanomaterials, including Pd/Co, Pd/Ru, Pd/Au, Pd/Fe, Au/Pt, Au/Pd, Cu/Ag, Co/Rh, Pd/Pt, Cu/Fe, Ag/Fe, Ni/Cu, and others, have been obtained in this vein [15-23].

The impact of BNP structure on their physicochemical and operational qualities, as well as the creation of a link between the synthesis technique and structure, are both basic and practical research topics. In this context, the discovery of ways for producing bimetallic NPs and stabilizing them, as well as the identification of potential applications, is of critical practical importance.

2. Materials and Methods

ChS *Bombyx mori*, with a molecular mass of 200×10^3 and a degree of deacylation of 70%, was employed to make stabilized bimetallic NPs. Metal salts such as $CoCl_2$, $CuSO_4$ and $AgNO_3$ were utilized because they were "chemically pure".

The kinetic parameters were investigated using a Litesizer 100 device (Anton Paar GmbH, Austria), which is used to calculate particle size using the Einstein-Stokes equation's diffusion coefficient. A single frequency laser diode with a 40 mW output produces a 658 nm laser.

The method of static and dynamic light scattering (photon correlation spectroscopy) - DLS - was used to measure the size of composites. The range of measured dimensions is in the range from fractions of nm to 5-10 microns. The power of the analyzer's laser is in the range of 2 mW-35 mW. Photocor analyzers have a mode of automatic measurements, processing and presentation of analysis results.

A SPECORD 210 spectrophotometer was used to conduct UV spectroscopic experiments in the range of 190 nm-1000 nm. Photometry UV accuracy using potassium dichromate according to Ph. Eur. 0.01.

3. Results and Discussion

The approach [14] was used to make chitosan-stabilized bimetallic nanoparticles (BNPs) in the presence of a reducing agent, $NaBH_4$. Metal ions were totally reduced and their number was 5±0.5% for all samples, according to the findings of spectral analysis of the mass fraction of metals.

3.1 The Studies the Kinetic Parameters of BNPs - Cu/Ag and Co/Ag

The hydrodynamic dimensions, diffusion coefficients, and polydispersity index of chitosan stabilized bimetallic nanoparticles have all been determined (Table 1).

Table 1. The effect of synthesis time on the particle size of chitosan stabilized bimetallic particles. 2.5 micron d (ChS)

#	BNPs samples	$[NaBH_4]\times10^{-4}$, mol	d, nm				Δd, nm
			3 min	6 min	9 min	12 min	
1	$Cu^{2+}/Ag^{+}=2:1$	1.3	227	235	231	224	230
2	$Cu^{2+}/Ag^{+}=2:1$	2.0	186	182	177	179	180
3	$Cu^{2+}/Ag^{+}=2:3$	2.0	246	264	267	260	260
4	$Co^{2+}/Ag^{+}=1:1$	2.6	199	218	212	200	207

The size of polymer-stabilized nanoparticles falls by around 10 times the size of polymer macromolecules during the synthesis of bimetallic nanoparticles in the presence of chitosan, according to studies of the hydrodynamic diameters of BNPs. The data also show that BNPs develop quickly, since the particle diameter does not vary from 3 to 12 minutes in any of the systems studied, and the average particle diameter is 180 nm-270 nm. It should be mentioned that the polydispersity indices in all of the examined systems of polymer-stabilized Me^{2+}/Ag^{+} BNPs are close to each other and, as a result, fall from 0.342 to 0.12±0.04 (Table 2).

This might be attributed to the disruption of intramolecular and intermolecular H-H and electrostatic bonds in chitosan solutions, as well as participation in metal nanoparticle stabilization. The data obtained from the DLS measurements are also close to the Litesizer results and range from 0.296 to 0.338.

As a result, it was discovered that the value of the diffusion coefficient of chitosan reduces by around 10 times after the stabilization of bimetallic nanoparticles. Furthermore, it was shown that the diffusion coefficient of chitosan stabilized bimetallic NPs is inversely related to the polydispersity index and particle diameter. Over example, the results in Table 3 show that for 3-12 minutes, the values of the diffusion coefficient of the particles of the tested samples are almost the same. DC sample #2 has a comparatively high flow rate of 2.71 cm^2/s, and the IP=0.12±0.04 and d=180 nm particle sizes are tiny, respectively.

The study of the prolongation effect of polymeric materials on drugs is of particular interest, which can be evaluated by modern physical methods [24]. The UV spectroscopy method has been used to study the kinetics of the release of ChS particles stabilized by BNP from the film, in which the absorption intensity is directly proportional to the number of electronic transitions or the concentration of the substance under study. The kinetics of this process can be considered as the diffusion of particles into an aqueous medium accompanied by conformational transitions of the polymer matrix leading to dissolution (Figure 1a,b).

Table 2. The effect of synthesis time on the index polydispersity (IP) of chitosan stabilized bimetallic particles. 0.342 IP (ChS)

#	BNPs samples	index polydispersity				ΔIP (by Litesizer)	IP (by DLS)
		3 min	6 min	9 min	12 min		
1	$Cu^{2+}/Ag^{+}=2:1$	0.25	0.16	0.18	0.21	0.20±0.04	0.314
2	$Cu^{2+}/Ag^{+}=2:1$	0.14	0.08	0.16	0.16	0.12±0.04	0.296
3	$Cu^{2+}/Ag^{+}=2:3$	0.23	0.19	0.26	0.26	0.22±0.03	0.326
4	$Co^{2+}/Ag^{+}=1:1$	0.11	0.15	0.21	0.25	0.18±0.06	0.338

Table 3. The effect of synthesis time on the diffusion coefficient (DC) of chitosan stabilized bimetallic particles. 0.2 cm^2/s DC (ChS)

#	BNPs samples	diffusion coefficient				ΔDC, cm^2/s
		3 min	6 min	9 min	12 min	
1	$Cu^{2+}/Ag^{+}=2:1$	2.16	2.08	2.11	2.18	2.13
2	$Cu^{2+}/Ag^{+}=2:1$	2.63	2.70	2.76	2.73	2.71
3	$Cu^{2+}/Ag^{+}=2:3$	2.47	2.25	2.31	2.45	2.37
4	$Co^{2+}/Ag^{+}=1:1$	1.99	1.85	1.83	1.88	1.90

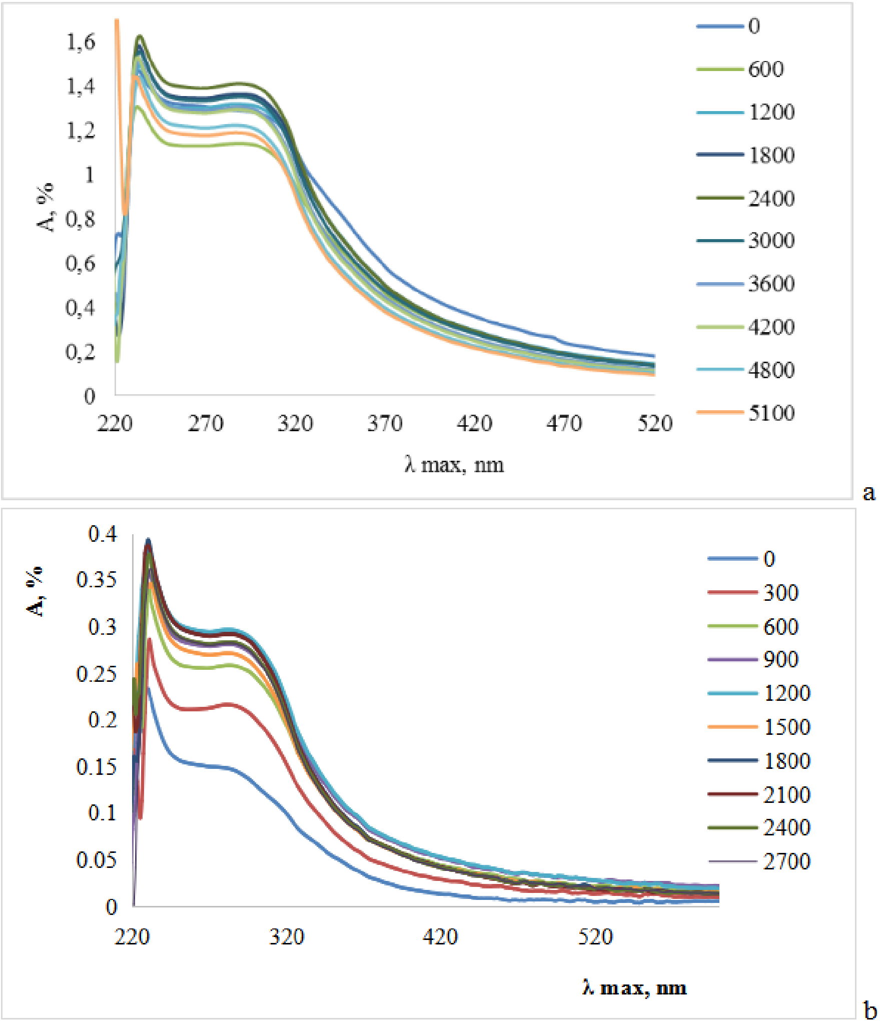

Figure 1. UV spectra of the release kinetics of chitosan stabilised bimetallic nanoparticles from the film of samples 3 (a) and 4 (b) with an interval of 10 minutes

Based on the results of the study, the diffusion coefficient of the BNP release process from the film in a medium of 2% CH_3COOH was estimated. To estimate the diffusion coefficient, we used the formula described by Fick's second law, which is given below:

$$\frac{dc}{dt} = D\frac{d^2c}{dx^2} \qquad (1)$$

$$c(x,t) = \frac{A}{\sqrt{t}}\exp\left(\frac{-x^2}{4Dt}\right) \qquad (2)$$

where c is the concentration of the solution, t is time, and D is the diffusion coefficient.

It follows that during the diffusion of polymer-stabilized BNP in an acidic medium there is a change in the intensity of the optical density of the solvent - CH_3COOH, which is directly proportional to the concentration of the dissolved substance. Fixing the change in absorption intensity over time of diffusion into the solvent, we determined the diffusion coefficients for samples #3 and #4, which are 2.723×10^{-7} cm^2/s and 4.817×10^{-8} cm^2/s, respectively.

3.2 UV Spectroscopic Studies

In order to research the structure of chitosan stabilized BNPs, we carried out UV studies (Figures 2 and 3).

The absorption bands of copper (II) ions are entirely decreased at 700 nm-900 nm in the spectra of the samples ChS-Cu/Ag examined. Cu NPs, on the other hand, generate a wide absorption band at 200 nm-300 nm that coincides with the absorption bands of chitosan's amin and acetamide groups. It's worth noting that the absorption band at 425 nm, which is typical of Ag NPs, is only seen in the spectra of sample #1. This might imply that Ag NPs are on the exterior of the sample, acting as a shell, whereas Cu NPs comprise the center. The absorption bands of Ag NPs are not evident in samples #2 and #3, despite the fact that the quantity of NPs is 5%. Ag NPs are most likely the center of these samples, with Cu NPs forming a shell around them.

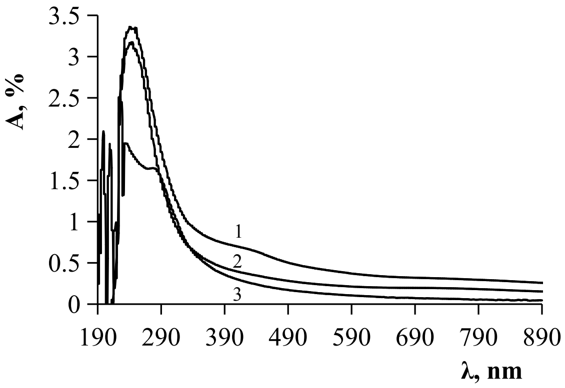

Figure 2. UV-spectra of ChS stabilized BNPs Cu/Ag: (1) $Cu^{2+}/Ag^{+}=2:1$, $[NaBH_4]$: 1.3×10^{-4} mol; (2) $Cu^{2+}/Ag^{+}=2:1$, $[NaBH_4]$: 2.0×10^{-4} mol; (3) $Cu^{2+}/Ag^{+}=2:3$, $[NaBH_4]$: 2.0×10^{-4} mol

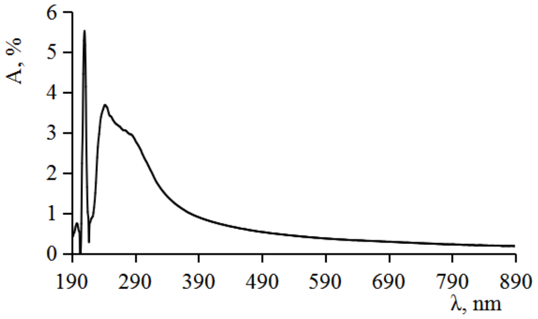

Figure 3. UV-spectra of ChS stabilized BNPs Ag/Co: $Co^{2+}/Ag^{+}=1:1$, $[NaBH_4]$: 2.6×10^{-4} mol

There is no absorption band of cobalt (II) ions at 500 nm in the spectra of sample #4, nor is there an absorption band of Ag NPs at 275 nm-600 nm. However, at 200 nm-206 nm, a significant absorption band develops, which is characteristic of Co NPs. This is most likely owing to the fact that spherical BNPs are generated under the specified synthesis conditions, with Ag NPs in the core and Co NPs in the shell. The results are consistent with those seen in the literature [15].

4. Conclusions

In conclusion, the hydrodynamic characteristics of chitosan stabilized bimetallic NPs - Cu/Ag and Co/Ag - produced under different synthesis circumstances have been determined. It has been discovered that the hydrodynamic properties of BNPs do not change significantly between 3 minutes to 12 minutes. A link has been established between the diffusion coefficient values and the polydispersity index, as well as the diameters of stabilized bimetallic nanoparticles.

Conflict of Interest

There is no conflict of interest.

References

[1] Cheng, H., Zhu, Q., Wang, A., et al., 2020. Composite of chitosan and bentonite cladding Fe-Al bimetal: Effective removal of nitrate and by-products from wastewater. Environmental Research. 184, 109336.
DOI: https://doi.org/10.1016/j.envres.2020.109336

[2] Pomogailo, A.D., Dzardimalieva, G.I., 2015. Metal-polymer hybrid nanocomposites. Moscow. Nauka. 494. (In Russian)

[3] Srinoi, P., Chen, Y.T., Vittur, V., et al., 2018. Bimetallic nanoparticles: enhanced magnetic and optical properties for emerging biological applications. Applied Sciences. 8, 1106.
DOI: https://doi.org/10.3390/app8071106

[4] Toshima, N., Yonezawa, T., 1998. Bimetallic nanoparticles-novel materials for chemical and physical applications. New Journal of Chemistry. 22, 1179-1201.

[5] Mustieles Marin, I., Asensio, J.M., Chaudret, B., 2021. Bimetallic Nanoparticles Associating Noble Metals and First-Row Transition Metals in Catalysis. ACS Nano. 15(3), 3550-3556.
DOI: https://doi.org/10.1021/acsnano.0c09744

[6] Loza, K., Heggen, M., Epple, M., 2020. Synthesis, Structure, Properties, and Applications of Bimetallic Nanoparticles of Noble Metals. Advanced Functional Materials. pp. 1909260.
DOI: https://doi.org/10.1002/adfm.201909260

[7] Dang-Bao, T., Pla, D., Favier, I., et al., 2017. Bimetallic Nanoparticles in Alternative Solvents for Catalytic Purposes. Catalysts. 7(7), 207-240.
DOI: https://doi.org/10.3390/catal7070207

[8] Sharma, G., Kumar, A., Sharma, S., et al., 2017. Novel development of nanoparticles to bimetallic nanoparticles and their composites: A review. Journal of King Saud University - Science. S1018364717303518.
DOI: https://doi.org/10.1016/j.jksus.2017.06.012

[9] Hillary, K.T., 2022. Bimetallic complexes; A mini review of their synthesis, and potential antitumor activities. https://www.researchgate.net/publication/332208732. (Accessed on 24 April 2022).

[10] Arora, N., Thangavelu, K., Karanikolos, G.N., 2020.

Bimetallic Nanoparticles for Antimicrobial Applications. Frontiers in Chemistry. 8, 412.
DOI: https://doi.org/10.3389/fchem.2020.00412

[11] Padilla-Cruz, A.L., Garza-Cervantes, J.A., Vasto-Anzaldo, X.G., et al., 2021. Synthesis and design of Ag-Fe bimetallic nanoparticles as antimicrobial synergistic combination therapies against clinically relevant pathogens. Scientific Reports. 11, 5351.
DOI: https://doi.org/10.1038/s41598-021-84768-8

[12] Srinoi, P., Chen, Y.T., Vittur, V., et al., 2018. Bimetallic nanoparticles: enhanced magnetic and optical properties for emerging biological applications. Applied Sciences. 8, 1106.
DOI: https://doi.org/10.3390/app8071106

[13] Velpula, S., Beedu, S.R., Rupula, K., 2021. Bimetallic nanocomposite (Ag-Au, Ag-Pd, Au-Pd) synthesis using gum kondagogu a natural biopolymer and their catalytic potentials in the degradation of 4-nitrophenol. International Journal of Biological Macromolecules. 190, 159-169.
DOI: https://doi.org/10.1016/j.ijbiomac.2021.08.211

[14] Vokhidova, N.R., Rashidova, S.S., 2021. The influence of synthesis conditions on the film morphology of chitosan-stabilized silver nanoparticles. Polymer Bulletin. pp. 1-18.
DOI: https://doi.org/10.1007/s00289-021-03669-y

[15] Zaleska-Medynska, A., Marchelek, M., Diak, M., et al., 2016. Noble metal-based bimetallic nanoparticles: the effect of the structure on the optical, catalytic and photocatalytic properties. Advances in Colloid and Interface Science. 229, 80-107.
DOI: http://dx.doi.org/10.1016/j.cis.2015.12.008

[16] Srinoi, P., Chen, Y.T., Vittur, V., et al., 2018. Bimetallic Nanoparticles: Enhanced Magnetic and Optical Properties for Emerging Biological Applications. Applied Sciences. 8(7), 1106-1138.
DOI: https://doi.org/10.3390/app8071106

[17] Ferrando, R., Jellinek, J., Johnston, R.L., 2008. Nanoalloys: From theory to applications of alloy clusters and nanoparticles. Chemical Reviews. 108, 845-910.
DOI: https://doi.org/10.1021/cr040090g

[18] Gilroy, K.D., Ruditskiy, A., Peng, H.C., et al., 2016. Bimetallic nanocrystals: syntheses, properties, and applications. Chemical Reviews. 116, 10414-10472.
DOI: https://doi.org/10.1021/acs.chemrev.6b00211

[19] Lu, H., Li, Y., Wang, Y., et al., 2019. Magnetic polyelectrolyte complex (PEC)-stabilized Fe/Pd bimetallic particles for removal of organic pollutants in aqueous solution. Materials Research Express. 6, 096113.
DOI: https://doi.org/10.1088/2053-1591/ab336e

[20] Diaz, C., Valenzuela, M.L., Bobadilla, D., 2013. Bimetallic Au/Ag metal superstructures from macromolecular metal complexes in solid-state. Journal of the Chilean Chemical Society. 58(4), 1994-1997.
DOI: http://dx.doi.org/10.4067/S0717-97072013000400019

[21] Keshipour, S., Sahra, S.M., 2017. Chitosan supported bimetallic Pd/Co nanoparticles as a heterogeneous catalyst for the reduction of nitroaromatics to amines. Advances in Environmental Technology. 1, 59-65.
DOI: https://doi.org/10.22104/aet.2017.501

[22] Wu, D., Kusada, K., Kitagawa, H., 2016. Recent progress in the structure control of Pd-Ru bimetallic nanomaterials. Science and Technology of Advanced Materials. 17(1), 583-596.
DOI: https://doi.org/10.1080/14686996.2016.1221727

[23] Yang, Ch., Ko, B.H, Hwang, S., et al., 2020. Overcoming immiscibility toward bimetallic catalyst library. Science Advances. 6(17), eaaz6844.
DOI: https://doi.org/10.1126/sciadv.aaz6844

[24] Sintzel, M.B., Bernatchez, S.F., Tabatabay, C., et al., 1996. Biomaterials in ophthalmic drug delivery. European Journal of Pharmaceutics and Biopharmaceutics. 42(6), 358-374.

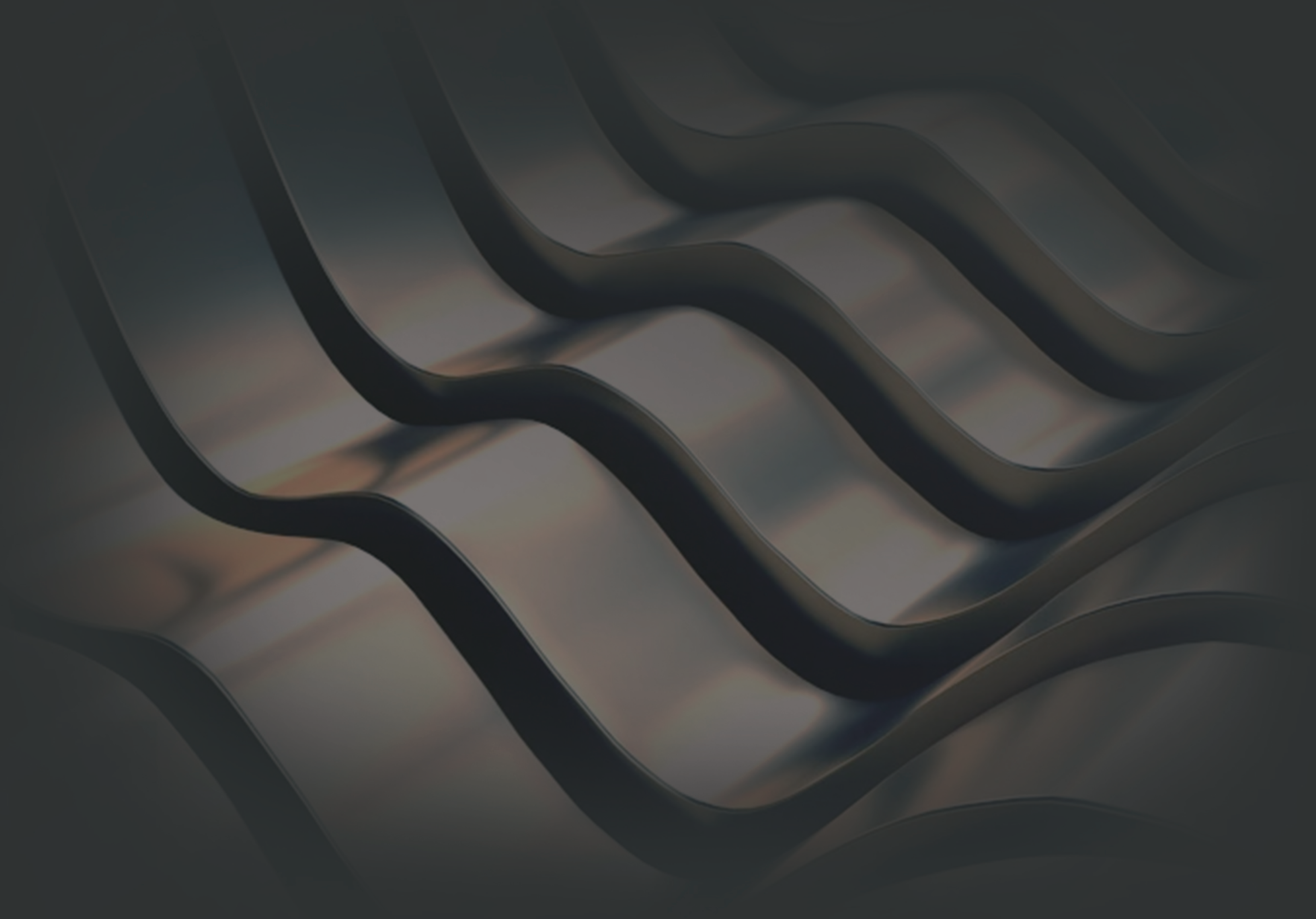

BILINGUAL
PUBLISHING CO.
Pioneer of Global Academics Since 1984

Tel:+65 65881289
E-mail: contact@bilpublishing.com
Website:ojs.bilpublishing.com

2630-5135
01
9 772630 513229